

# Mechanical properties of Thermoplastic/Thermoset interphases

Dissertation presented by

**Mathieu Bois**

for obtaining the Master's degree in

**Ingénieur civil en chimie et science des matériaux**

Supervisor(s)

**Christian BAILLY**

Reader(s)

**Thomas PARDOEN, Quentin VOLEPPE**

Academic year 2015-2016

# Contents

---

<b>1</b>	<b>State of the art</b>	<b>7</b>
1.1	Thermoset Composite Welding (TCW) . . . . .	7
1.2	Thermodynamics of phase separation in polymers . . . . .	10
1.3	Thermodynamics and kinetics of inter-diffusion and swelling . . . . .	15
1.4	Fracture mechanics of interphases . . . . .	17
1.4.1	Basics of fracture mechanics in homogeneous media . . . . .	17
1.4.2	Damage properties of interfaces . . . . .	21
1.5	Physico chemistry and damage properties of TS-TP interphases . . . . .	25
<b>2</b>	<b>Methods and Experiments</b>	<b>29</b>
2.1	Materials . . . . .	29
2.1.1	RTM6 epoxy resin properties . . . . .	29
2.1.2	PEI . . . . .	29
2.1.3	PETT . . . . .	30
2.2	Preparation . . . . .	30
2.2.1	RTM6 - curing procedure . . . . .	30
2.2.2	Polymer blends . . . . .	32
2.2.3	Press: thin films . . . . .	33
2.2.4	Laser patterning . . . . .	33
2.2.5	3D printing patterning . . . . .	34
2.2.6	Interphases . . . . .	36
2.2.7	Surface preparation by microtomy . . . . .	37
2.3	Characterization . . . . .	38
2.3.1	Physico-chemical characterization . . . . .	38
2.3.2	Mechanical characterization . . . . .	40
<b>3</b>	<b>Study of plane interphases</b>	<b>45</b>
3.1	Characterization of the interphases and discussion . . . . .	46
3.2	Mechanical tests results . . . . .	50
<b>4</b>	<b>Influence of the patterning</b>	<b>57</b>
4.1	Laser patterning . . . . .	58
4.2	Patterning via 3D printing . . . . .	61
4.3	Characterization of the interphases . . . . .	61

## List of Figures

---

1.1	Comparison between mechanical fastening and adhesive bonding . . .	7
1.2	Scheme of the Thermoplastic/thermoset cocuring . . . . .	9
1.3	Prepreg layup with an additionnal layer of thermoplastic . . . . .	10
1.4	Toughness of TP-TS blends with different thermoplastics used as a function of the weight percentage of thermoplastic . . . . .	11
1.5	The three different fractures modes considered in linear elastic fracture mechanics . . . . .	11
1.6	Concentration profiles obtained for the methanol-PMMA system . . .	17
1.7	The three different fractures modes considered in linear elastic fracture mechanics . . . . .	18
1.8	Ce qui apparait dans la table des igrures . . . . .	19
1.9	Scheme summarizing of the different areas surrounding the crack tip. .	20
1.10	Schemes of different morphological profiles with their respective chemical composition . . . . .	21
1.11	Scheme of a crack at the interface between two different materials . . .	23
1.12	$\sigma_C$ as a function of $\delta$ for two interfaces having the same adhesive energy	23
1.13	Different interaction mechanisms between a crack and an interface. .	24
1.14	$\sigma_C$ as a function of $\delta$ for two interfaces having the same adhesive energy	25
1.15	Scheme of the interphase morphologies formed by the curing of an epoxy resin on top of a TP film . . . . .	27
1.16	TEM cliches of a DGEBA-MCDEA/PPE interphase at either low and high conversion of the resin . . . . .	27
2.1	Diamine hardeners (top) and multifunctional epoxyde (bottom) forming the RTM6 resin synthetized by Hexcel. . . . .	29
2.2	Reaction mechanism occurring during the epoxy resin reticulation . .	30
2.3	Polyetherimide PEI structure of PEI Ultem 1000 synthetized by Sabic .	30
2.4	Curing cycle used, with the corresponding simulated and real conversion of the thermoset resin . . . . .	32
2.5	Scheme of 3D printer for Fuel Deposition Modeling. . . . .	35
2.6	Image of the sidecut of a 3D printed PETT film . . . . .	36
2.7	Picture of the software used for the 3D printing : short view of the possible parameters available to tune the printing . . . . .	36
2.8	Scheme of the profile vue of the samples prepared for SENB preparation	38

## LIST OF FIGURES

---

2.9	DSC curve of a PETT sample . . . . .	38
2.10	Example of a DSC (a) and a TGA (b) curve . . . . .	39
2.11	SCHEMA SENB . . . . .	42
2.12	Experimental setup of the SENB test . . . . .	42
2.13	Load-unload plotting of P as a function of the penetration depth of the nano-indent . . . . .	43
2.14	indent $pe_i$ . . . . .	44
2.15	Experimental setup of the compressions tests . . . . .	45
2.16	Illustration of the barreling effect . . . . .	45
3.1	PETT RTM6 - PEI RTM6 interface comparison . . . . .	46
3.2	Optical images of PEI/RTM6 cured homogeneous blends. . . . .	48
3.3	Optical images of PETT/RTM6 cured homogeneous blends. . . . .	49
3.4	Ce qui apparait dans la table des figures . . . . .	50
3.5	Evolution of the length of the co-continuous area as a function of the resin conversion . . . . .	51
3.6	Compression results . . . . .	52
3.7	Compression test : elastic limit . . . . .	52
3.8	Load applied on the sample with the tip as a function of its depth of penetration . . . . .	53
3.9	Load applied on the sample with the tip as a function of its depth of penetration . . . . .	54
3.10	Nano-indentation results compared with the compression results . . . . .	54
3.11	Picture of a broken SENB sample. . . . .	55
3.12	Picture of a broken SENB sample. . . . .	56
4.1	Scheme of the aimed TP-TS interphase with roughness . . . . .	57
4.2	Scheme of the path followed by the laser . . . . .	59
4.3	Picture of a resin cured upon PEI with a pattern on its surface . . . . .	60
4.4	Several patterns performed with the laser (right), where only the beam power varies . . . . .	60
4.5	Scheme of the SENB samples preparation, with patterned PETT films . . . . .	61
4.6	Detailed scheme of a PETT film . . . . .	62
4.7	Picture of a broken SENB sample . . . . .	62

## List of Tables

---

2.1	RTM6 gelling time as a function of the curing temperature . . . . .	32
3.1	List of the samples prepared for the analysis of the influence of the initial conversion of the resin at the beginning of the co-curing on the length of interdiffusion. . . . .	50
3.2	List of the samples prepared for the nanoindentation test . . . . .	53

## Introduction

---

During the past five years the Boeing 787 and the Airbus A350 were commissioned. Both of them are made of composites for more than a half of the structure in mass [1]. From the A380 with 23 % [2] to the A350, there is a tendency to increase the composite proportion in aeronautics. It implies that many researches are carried out nowadays in order to improve the composites performances, and one of the topics is the assembly of carbon fiber reinforced polymers (CFRP) pieces.

In this context, this master thesis is related to a promising joining method for the assembly of composite parts for aeronautical applications, namely thermoset composite welding (TCW). This joining method could indeed be used as an alternative to more commonly used techniques such as riveting or adhesive bonding. Riveting, initially designed for metallic materials, is not well suitable for composites structures. Indeed, the presence of the rivets has two main disadvantages: it adds weight to the structure and necessitates the drilling of holes. These holes act as stress concentration points in the structures [3]. Because composites are brittle by nature, it becomes necessary to reinforce these structures in the surroundings of the joint : this local reinforcement involves extra weight once again as well as a conservative design of the joints, which is detrimental to the use of composites in aircrafts. Thermoset Composite Welding, consisting in welding two thermoset composites using thermoplastic layers at their surface, would alleviate these unnecessary constraints. However, the interphases formed during TCW between the thermoset (TS) and the thermoplastic (TP) layer usually present poor mechanical properties, especially in terms of damage resistance.

The aim of this work is to study the interphases generated by the interdiffusion and phase separation between a TS resin used in aeronautics and a TP when subjected to a curing cycle, in order to improve their fracture resistance. The interdiffusion at a TS/TP interphase is a complex process involving time varying swelling and disentanglement of polymer chains due to the increasing molecular weight of the TS reactive species upon curing. It has already been studied by Dumont et al. [4] in the case of a TP with a lower glass transition temperature ( $T_g$ ) than the curing temperature. It has also been studied in the case of a high  $T_g$  TP, poly(ether imide), in the work of Quentin Voleppe. However, the corresponding mechanical properties

have only been studied partially in the case of the high  $T_g$  TP. The project first finalizes the mechanical study of the interphases based on poly(ether imide) (PEI) started in the work of Quentin Voleppe. Second, it starts the mechanical characterization of the interphases based on a low  $T_g$  amorphous polymer derived from poly(ethylene terephthalate) (PETT). Moreover, the influence of the surface roughness of the TP layer is considered as an additional parameter to improve the mechanical response, and especially the fracture toughness, of the corresponding interphases.

# 1 State of the art

## 1.1 Thermoset Composite Welding (TCW)

### Assembly techniques

The joining of composite parts appeals to two techniques: mechanical fastening and adhesive bonding. Mechanical fastening, and more specifically riveting, is the main method used in aeronautics. An advantage to rivets is that parts can be disassembled for revision. This joining method is also supported with adhesive bonding. However, several drawbacks come with it [5]:

- Riveting adds weight to the structure, while one of the main reasons for the use of composites is mass savings.
- Low processing speed due to many steps
- The drilled holes act as stress concentration points, as illustrated in figure 1.1, which can be critical given the fact that carbon fiber reinforced polymers (CFRP) show a brittle behavior, especially due to the thermoset polymer matrix.
- In addition to the previous point, the stress repartition among the CFRP, especially at the fiber cut-out where the fastener is localised, makes the structure more likely to crack at this location.

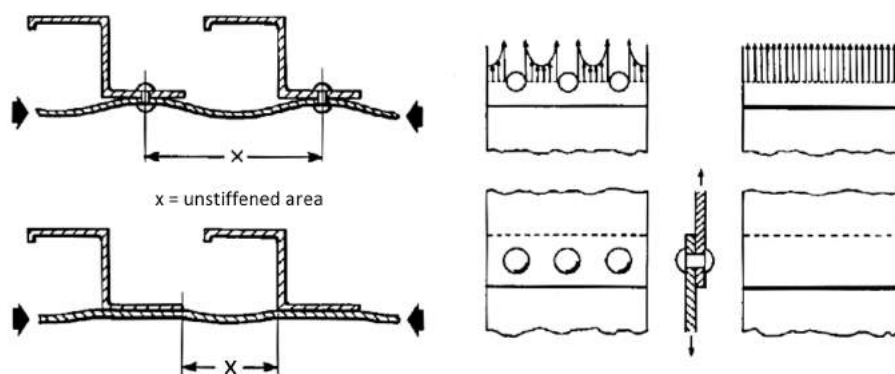


Figure 1.1: Comparison between the stress distribution in mechanically fastened and adhesively bonded joints.

Adhesive bonding consists in using a third intermediate layer between the parts that have to be assembled. An efficient way to assemble parts keeping strong mechanical

properties is to use a thermoset polymer. The main interesting point is that the connection between the assembled parts is better since all the shared surface between the parts is continuously connected via the thermoset polymer, initially liquid and filling the available volume in between. Indeed, avoiding the presence of holes induced by rivets leads a more homogeneous stress distribution among the joint compared to mechanically fastened structures, as illustrated in Figure 1.1. Finally, the parts that have to be assembled can be made of dissimilar materials and can differ in shape as well due to the liquid filling. However, this joining method also presents drawbacks [5]:

- The interface strength is very dependent on the initial surface. It requires an initial preparation of the surface to avoid impurities and surface defects which could lead to a weakening of the assembly . Indeed, localised marks of fat for instance induce poor adhesion of the adhesive to the surface. This preparation is time consuming and expensive.
- The mechanical properties of the adhesive depend on temperature. At high temperatures, there is a drop of the properties, limiting its use to temperatures below 200°C
- Adhesive bonding is effective in compression and shear, which is why the joints must be designed in order for the adhesive to undergo only these types of load.
- The reliability of the mechanical tests for the adhesion make this process hard to be approved by organisms providing certifications.

More recently, another technology has been considered as an alternative to riveting and adhesive bonding, namely "Thermoset Composite Welding".

### **Thermoset Composite Welding**

Thermoset composite welding is a two step process. It consists first in depositing and curing the resin (PREPEG, TSMC) on a glassy thermoplastic film. Part of the thermoplastic, over a given thickness, interacts with the resin (swelling, diffusion), while the rest remains "unchanged" (changer la formulation). At the end of this step, the joint is composed of a succession of three different layers : a pure thermoplastic region, a pure thermoset region, and in between a microstructure gradually changing with the concentration of TP (or TS) [5]. This is illustrated in Figure 1.2. The second step consists in joining two such parts thanks to the presence of the remaining pure

thermoplastic regions, by heating [5]. The heat partially fuses the thermoplastic layers of each part, allowing a mixing of the two thermoplastic layers at a temperature higher than the  $T_g$ . After cooling down, the welding is achieved and the mechanical properties at the initial TP-TP interface are identical to the ones of the bulk TP.

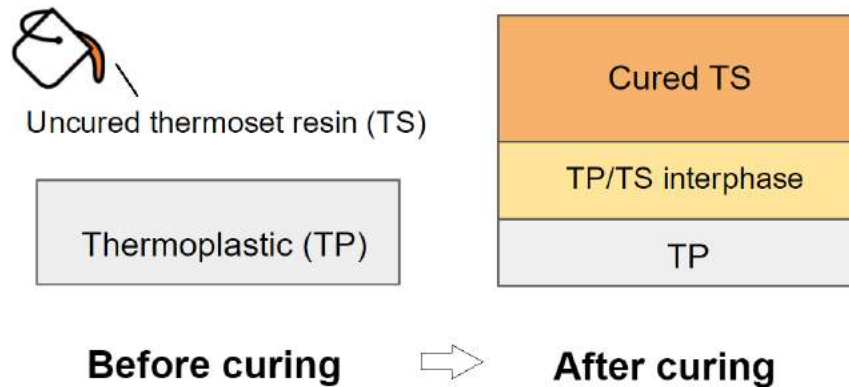


Figure 1.2: Scheme of the global obtained sample during the Thermoplastic/thermoset cocuring. At the left, the uncured thermoset resin is poured on top of the thermoplastic layer. Upon curing, interdiffusion occurs, forming an intermediate layer between the pure cured thermoset layer and the unchanged thermoplastic layer.

The TP and the TS must be chosen accordingly to the application. Moreover, the chosen pair allows to tune the damage properties of the joint [6]. Indeed, every single TP-TS pair gives a specific microstructure depending on the thermodynamic parameters. From the beginning at the contact TP-TS interdiffusion occurs between the thermoplastic and the resin. Meanwhile, the resin is curing. The reticulation causes an molecular weight increase of the TS polymer chains, changing its properties. This leads to a microstructure specifically dependent on the TS-TP choice. Indeed, from the thermodynamics and kinetics explained later on, after the diffusion process which is quite fast compared to the time scale of the curing cycle, phase separation occurs [7]. The resulting phase separated morphology depends on the concentration and so on the distance from the initial interface. Since the mechanical properties rely on the morphology obtained, the advantage of such technique is that it is possible to play with all the parameters (choice of the materials, curing cycle, geometry of the initial interface) in order to reach a micro-structure with good mechanical properties [8]. Since the interphase is usually less resistant to crack propagation [7], improving its mechanical properties is of main importance. Finally, this technique can easily be implemented to already existing processes for preparing parts as showed in Figure 1.3, such as Resin Transfert Molding.

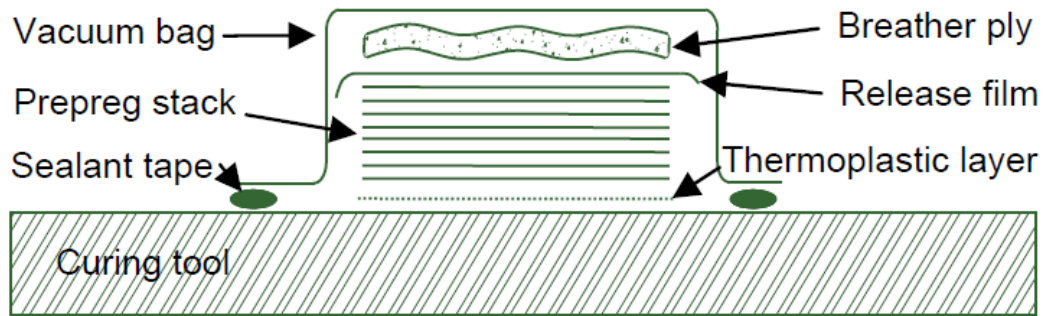


Figure 1.3: Prepreg layup with an additional layer of thermoplastic in the curing tool [5]

To conclude, thermoset composite welding is a promising way to joint CFRP parts getting rid of the drawbacks of the other methods such as stress concentration, added weight, number of steps, while maintaining competing mechanical properties. This process can also be implemented into already existing techniques such as resin transfer molding.

## 1.2 Thermodynamics of phase separation in polymers

Epoxy resin toughening via mixing of the resin with a thermoplastic has been demonstrated: Figure 1.4 shows the toughness of TP-TS blends with different thermoplastics used as a function of the weight percentage of thermoplastic [9]. It shows the interest of understanding polymer blends formation, especially the resulting microstructure. A lot of research and computation were done, especially for theoretical analysis of polymer mixing. The most known modelling comes from the work of Flory and Huggins, based on the liquid lattice theory, which is the starting point of the recent and more advanced theories. This section aims to describe this theory and what results we can find based on this simple model.

One starts with two different pure polymers A and B with respectively  $N_a$  and  $N_b$  molecules. The -liquid lattice- from Flory and Huggins is a lattice of well arranged sites in which atoms are included. Such liquid lattice is illustrated in Figure [10] [11] 1.5 [12].

It is a simplified model since liquids present a certain disorder. Before mixing, all the chains in one polymer have, in average, the same environment, since the polymer is pure. Then, for the mixing of two polymers, the free energy of mixing is given by

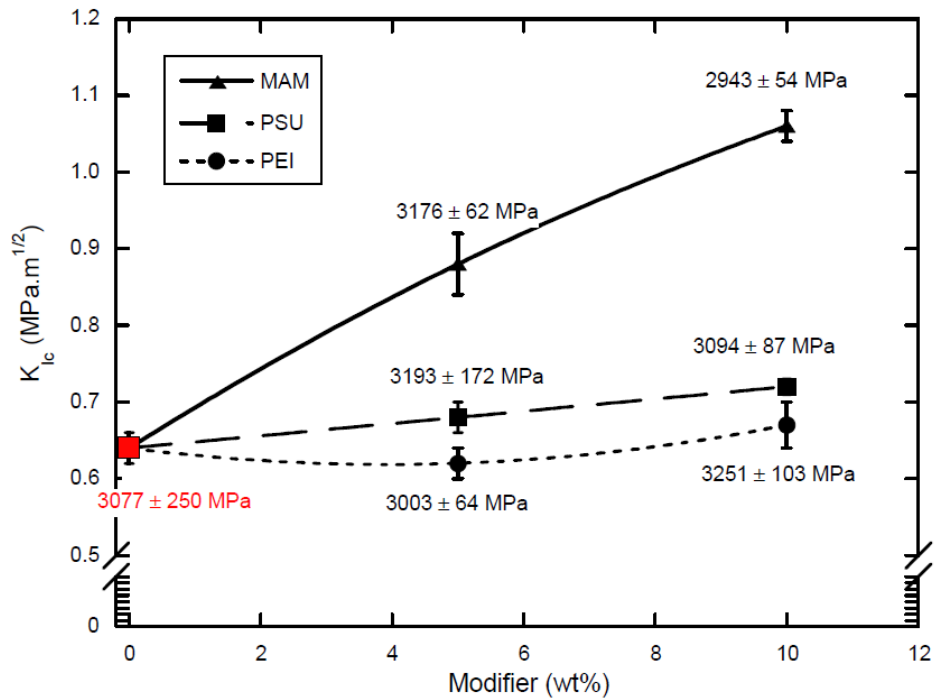


Figure 1.4: Toughness of TP-TS blends with different thermoplastics used as a function of the weight percentage of thermoplastic [9]

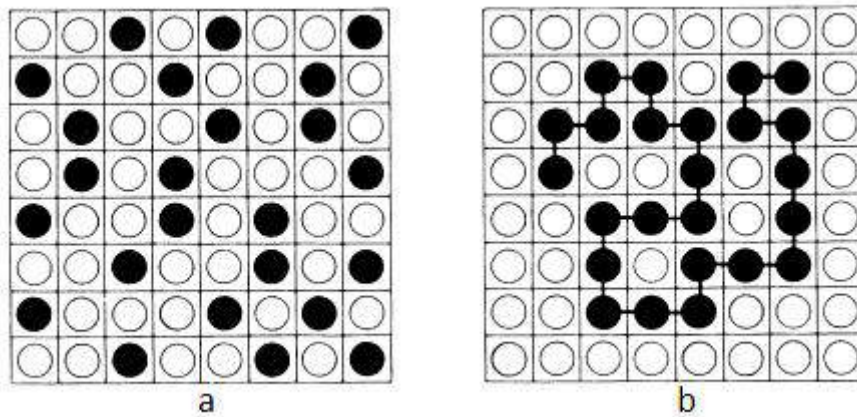


Figure 1.5: Scheme of the liquid lattice assumption for the Flory-Huggins model: the liquid is considered partially arranged into square domains occupied by atoms (picture a), themselves covalent bonded in the case of polymer chains (picture b). [12]

equation 1.1, which is expressed, in the most general case, as equation 1.2:

$$\Delta G_M = \Delta H_M - T\Delta S_M \quad (1.1)$$

$$\Delta G_M = \Delta H_M^{nonspecific} + \Delta H_M^{other} - T\Delta S_M^{configurational} - T\Delta S_M^{non-configurational} \quad (1.2)$$

The (numerous) hypotheses on which relies this model are [13]:

- The medium considered is a lattice delimited by squares containing atoms with identical dimension regardless of the type of atoms
- The entropy of mixing is only configurational, that is to say the entropy of mixing is only dependent on the organisation and arrangement of the molecules over the liquid lattice
- the enthalpy term includes only the non specific interactions that occur all the time, and not the specific interactions, neither the configurational energy differences which are first neglected.

#### Modeling of $\Delta H_M^{nonspecific}$

In equation 1.2,  $\Delta H_M^{nonspecific}$  is computed considering the interactions between molecular chains in contact with each other. To do so, the mixing enthalpy for one site  $\Delta H_M^{persite}$  is calculated, to finally reach the total mixing enthalpy over the volume by multiplying the mixing enthalpy for one site with the number of sites. During mixing, the environment changes and some of the old neighbours are replaced by new ones from the other polymer. The exchange energy is the change in energy occurring during the switching of two "elementary" sites. It is given by

$$w = \left( \frac{\epsilon_{11}}{2} + \frac{\epsilon_{BB}}{2} - \epsilon_{AB} \right) \quad (1.3)$$

which is, in the case of Van Der Walls interactions, in a simplified way :

$$w_{nonspecific} = \frac{1}{2} (\sqrt{\epsilon_{AA}} - \sqrt{\epsilon_{BB}})^2 > 0 \quad (1.4)$$

and thus lead to the mixing enthalpy per site for an exchange:

$$\Delta H_M^{persite} = zw = z \frac{1}{2} (\sqrt{\epsilon_{AA}} - \sqrt{\epsilon_{BB}})^2. \quad (1.5)$$

[13]. The mixing enthalpy of the whole volume is the probability for an exchange to occurs for a site, time the number of sites  $N_s = \frac{V_{total}}{V_{site}}$ , times the change in energy

involved for the switching. Knowing that the probability of a site to be exchanged is  $\Phi_A\Phi_B$  :

$$\Delta H_M^{nonspecific} = zN_s w \Phi_A \Phi_B \quad (1.6)$$

This term can also be defined as [14]:

$$\Delta H_M^{nonspecific} = kT \chi_{AB} N_A \Phi_B = kT N_A \Phi_B \cdot \frac{z \Delta w_{AB} X_A}{kT} \quad (1.7)$$

Where  $X_A$  is the degree of polymerisation of A, T the temperature and  $\chi_{AB}$  the so called Flory Huggins parameter including the change in energy  $\Delta w_{AB}$

### Modeling of $\Delta S_M^{configurational}$

Assuming that the mixing entropy only depends on the atoms apportionment over space with equal probabilities for each of the configurations, the mixing entropy is given by :

$$\Delta S_M = k \frac{\Sigma_M}{\Sigma_0} = -kN (x_a \ln(x_A) + x_b \ln(x_b)) \quad (1.8)$$

where  $N = N_A + N_B$  and  $x_i = \frac{N_i}{N}$ . However, chains are linked and the linking reduces the number of configurations available. From the work of Flory and Huggins, the new entropy is expressed as :

$$\Delta S_M = -kN (\Phi_A \ln(\Phi_A) + \Phi_B \ln(\Phi_B)) \quad (1.9)$$

[13]. Finally, the combination of the previous equations 1.2, 1.6 and 1.9 considering the hypothesis gives the so called Flory Huggins equation:

$$\frac{\Delta G_M}{N_s kT} = \chi_{AB} \Phi_A \Phi_B + \left( \frac{\Phi_A}{X_A} + \frac{\Phi_B}{X_B} \right) \quad (1.10)$$

[13]. It is also written, from equation 1.7 instead of equation 1.6:

$$\frac{\Delta G_M}{N_s kT} = \frac{\Phi_A}{X_A} \ln(\Phi_A) + \frac{\Phi_B}{X_B} \ln(\Phi_B) + \frac{k \chi_{AB}}{k \chi_A} \Phi_A \Phi_B \quad (1.11)$$

The numerous hypothesis make this theory quite unrealistic. For instance, a liquid possesses a certain disorder. However, this theory remains a base for further developments and allows to establish results [13]:

- the originally neglected  $\Delta S_M^{non-configurational}$  is dominant over  $\Delta S_M^{configurational}$

which is close from zero due to the high degree of polymerisation  $X$  ( $N=N_0/X$ ). From this the first result is that polymer blends are expected to be poorly miscible for either a high temperature ( $\Delta S_M$  or high molecular weight

- Also,  $\Delta H_M^{specific}$  was neglected, but as  $\Delta H_M^{nonspecific} > 0$ ,  $\Delta H_M^{specific}$  might be positive or negative, but only  $\Delta H_M^{specific}$  can favour the mixing.

Phase diagrams can be computed from the Flory Huggins equation and the miscibility conditions are given by:

$$\Delta G_M < 0 \quad (1.12)$$

$$\frac{\partial^2 G}{\partial \Phi^2} > 0 \quad (1.13)$$

[13]. From the two conditions 1.12 and 1.13 it is possible to determine the miscibility, depending on the parameters such the temperature or the degree of polymerisation of the species, and predict any phase separation, for instance spinodal decomposition. Phase diagrams are the most convenient way to illustrate the results.

In order to approach reality, instead of adding the terms  $\Delta S_M^{non-configurational}$  and  $\Delta H_M^{other}$  originally neglected, the Flory Huggins parameter includes these changes by adding terms to it, and in the general case:

$$\chi = \chi_H + \chi_S \quad (1.14)$$

where  $\chi_H$  is the originally considered Flory-Huggins parameter, and  $\chi_S$  is an added term for the non-combinatorial entropic contribution.

Some models predict that the Flory Huggins parameter is inversely proportional to the temperature [15]. These models can be supported with the phase field theory, numerically simulating the phase separation and providing potential morphologies [16]. However, the phase field theory is out of the scope of this master thesis.

Finally, the Flory-Huggins equation can be generalized to multi-component systems, i.e. systems including more than two different polymers. The related equation to this system is written :

$$\frac{\Delta G_M}{RT} = \sum_{i=1}^N \frac{\Phi_i}{X_i} \ln \Phi_i + \sum_{i<j}^N \chi_{ij} \Phi_i \Phi_j \quad (1.15)$$

[16].

To conclude, the Flory-Huggins parameter, despite numerous hypothesis, allows to determine good results such the fact that polymer blends are expected to be poorly miscible for either a high temperature or a high molecular mass. Also, this model remain a solid base for further and more accurate developments and is not limited to the mixing of only two different polymers.

### 1.3 Thermodynamics and kinetics of inter-diffusion and swelling

A well known classical model for diffusion is Fick's model. This model allows to determine for instance temperature gradient profiles or, for our concern, concentration gradients among a medium undergoing diffusion of molecules. As simple as this model is, it provides good results for media made of newtonian liquids. However polymers are viscoelastic, or in other words, non Newtonian liquids: the diffusion process is thus non Fickian, and involves phenomena such as swelling, which is an increase of volume of a thermoplastic penetrated by solvent molecules diffusing through it. It is however necessary to well understand the non-Fickian diffusion for many applications involving diffusion in polymers.

We can wonder what are the differences between the classical fickian diffusion and the non classical one, and what additional features are lead to such type of diffusion. To explain this, we consider the diffusion of a solvent in a thermoplastic, which is the case of the process in thermoset composite welding. The classical fickian model for diffusion gives in the case of a 1D diffusion:

$$J = -D \frac{\partial C}{\partial x} \quad (1.16)$$

$$\frac{\partial C}{\partial t} = -\frac{\partial J}{\partial x} = \frac{\partial}{\partial x} \left( D \frac{\partial C}{\partial x} \right), \quad (1.17)$$

in the 3D case, equation 1.16 turns into :

$$\vec{j} = -D \overrightarrow{grad}(C) \quad (1.18)$$

where  $C$  is the concentration of one of the two components of the system,  $D$  is their interdiffusion coefficient and  $J$  is the interdiffusion flux.

It is the simplest model for mass transport in two-component systems and the most frequently used due to its mathematical tractability. (describe terms of formulas).

The solution of equations 1.16 and 1.17 follows a scaling rule :

$$l \propto \sqrt{Dt} \quad (1.19)$$

Where  $l$  and  $t$  are characteristic length and time. Diffusion of polymers in their rubbery state, i.e. at temperatures above their  $T_g$ , follows quite well the Fickian rule, but differ from more classical Newtonian fluids since the diffusion coefficient is ruled by the reptation process, making it strongly dependent on the concentration and the volume fraction [17][18]. The scaling rule in the case of the reptation gives:

$$D \propto \frac{1}{\Phi^{1+\alpha}} \quad (1.20)$$

where  $1 < \alpha < 1.3$  and  $\Phi$  is the volume fraction.

In the case of a polymer in its glassy state, thermodynamic equilibrium is not satisfied anymore : the diffusion coefficient of the polymer-penetrant system is not constant as it depends not only on concentration as in the rubbery state but also on time. The two main mechanisms at the origin of time dependent nature of diffusion in a glassy polymer are the time varying pressure applied on the polymer by the solvent as it penetrates the polymer and stretches its chains progressively and the rearrangement of the polymer due to the viscoelastic relaxation of the chains [19]. It leads to a sharp diffusion front, as illustrated in Figure 1.6 [20].

To conclude, one can distinguish three different types of diffusions. For our concern, diffusion process at the interface between RTM6 and a TP are rather non linear in the case of a TP having a high  $T_g$ , so that it remains all the time in its glassy state, or appealing to the reptation mechanism coupled to Fickian diffusion in the case of a polymer above its  $T_g$ . Depending on the type of diffusion followed by the species among the interphase, the resulting concentration profile differs, while it partially rules the mechanical properties.

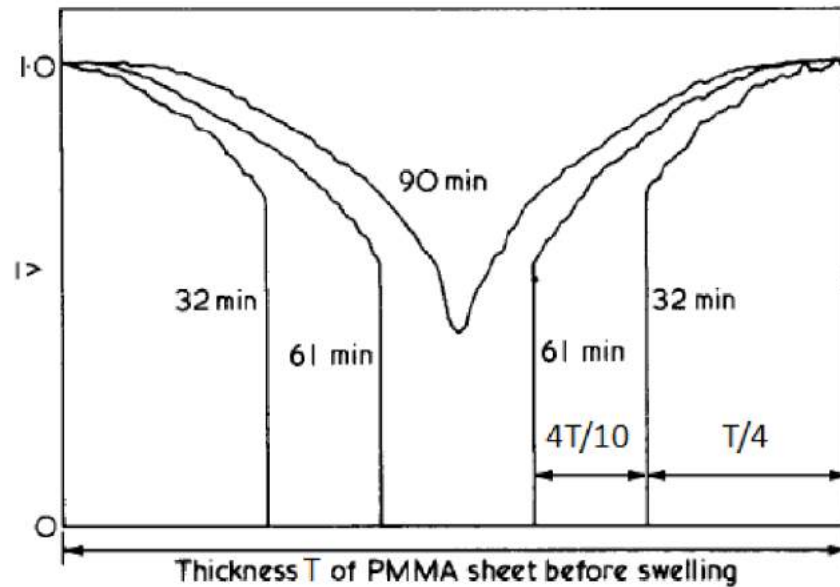


Figure 1.6: Concentration profiles obtained for the methanol-PMMA system at 52°C showing an abrupt interface in concentration [20]

## 1.4 Fracture mechanics of interphases

The stake of the TCW application to CFRP is to prevent crack propagation at the interface. This is why it is necessary to have a good knowledge of fracture mechanics: this section focuses on the basics of crack propagation in order to better understand the damaging of solid-solid interfaces described later on.

### 1.4.1 Basics of fracture mechanics in homogeneous media

Any defect such as a crack or a hole within a material produces a specific stress field around the defect when the material under loading. Linear elastic fracture mechanics LEFM can be defined considering the fact that material's elasticity is linear and isotropic [21].

- the crack is rectilinear.
- There exist 3 different crack opening modes, every crack propagation being a linear combination of these three modes, showed Figure 1.7 .

In LEFM, the general stress state around the crack tip is expressed for example in mode one as

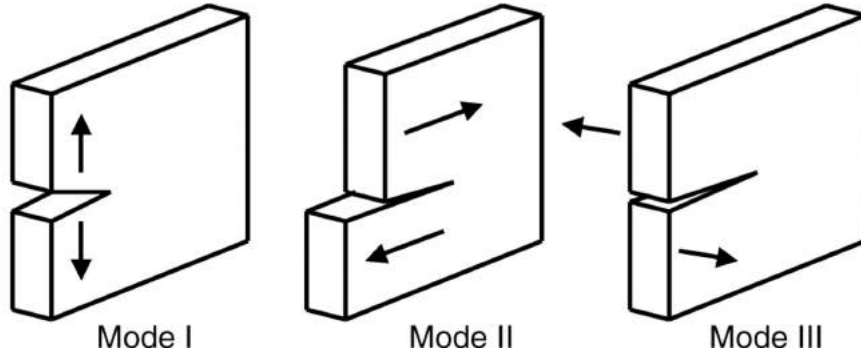


Figure 1.7: Scheme of the assumed 3 different modes of fracture in linear elastic fracture mechanism. [22]

$$\sigma_{ij}^I = \frac{K_I}{\sqrt{2\pi r}} f_{1ij}^I(\theta) + \sum_{n=2,3,\dots}^{\infty} C_n^I(K_I, a, \dots) r^{\frac{n}{2}-1} f_{nij}^I(\theta), \quad (1.21)$$

where  $K$  is the stress intensity factor which is a constant as well as  $C_n$ . Considering that equation, the stress field depends only on  $K$  and  $C_n$ , themselves depending on the configuration of the problem, such as the crack size *a.enitalique* and the loading. Generally  $K_I = \sigma^\infty Y \sqrt{a}$  where  $Y$  is only dependent on the geometry of the problem, and where  $\sigma^\infty$  is the loading [21].

#### Validity area: K-dominance zone

The terms of order  $n>1$  can be neglected for  $r/a<0.1$ , as showed Figure 1.8. On the other hand, close from the tip, in the order of  $r/a<0.03$ , since the dependence in  $1/\sqrt{r}$  makes the stresses diverging, at some point the stress is such that plastic deformation occurs, and this area undergoes non linear fracture mechanics. However, even in the area  $0.03<r<0.1$  LEFM is valid for area which undergoes non linear transformations that are small enough. This criteria, called small scale yielding, can be verified via the Von Mises criteria which stipulates that yielding occurs when :

$$\sqrt{\frac{1}{2}[(\sigma_x - \sigma_y)^2 + (\sigma_y - \sigma_z)^2 + (\sigma_z - \sigma_x)^2] + 3\tau_{xy}^2} = \sigma_0 \quad (1.22)$$

where  $\sigma_{x,y,z}$  and  $\tau_{xy}$  are the stresses and shear around the crack tip and  $\sigma_0$  the initial yield strength.

#### Energetic consideration

The problem can also be seen with an energetic approach. If one loads an elastic linear

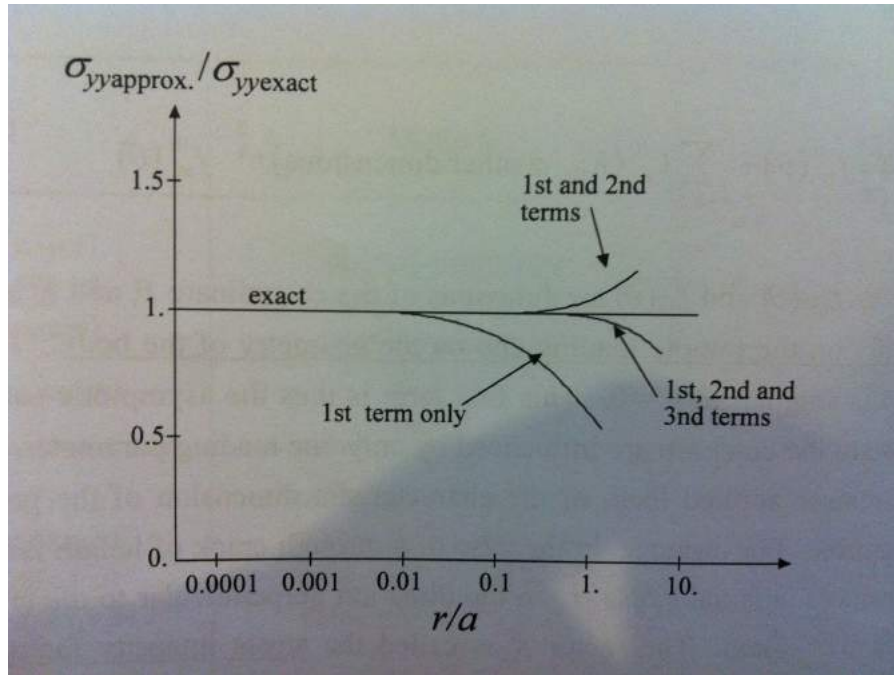


Figure 1.8: Ratio of the stress approximated by neglecting one or more terms in the equation 1.21 over the exact stress, as a function of  $r/a$ , where  $r$  is the distance in polar coordinates and  $a$  the crack length. In neglecting all the terms but the first order one, the computation of the stress field remain valid for  $r/a < 0.01$ . [21]

material with quasi static loading (to avoid inertia effects) producing a displacement  $h$  with an initial crack surface  $A$ : all the work provided to the sample will be stored in the sample by elastic deformation until the work exceeds the maximum amount of stored energy by this mechanism. The difference between the work provided and the maximum energy stored by elasticity is transferred to the crack area. So  $G$  is defined as the variation of the excess energy provided by the sample to the crack surface:

$$G = -\frac{\partial P}{\partial A} \quad (1.23)$$

where  $A$  is the crack surface and  $P$  the mechanical energy of the system.  $G$  and  $K$  are closely related. If the opening crack mechanism can be a combination of the 3 modes seen in Figure 1.7, in the case of LEFM via the following formula (neglecting further terms):

$$\sigma_{ij}^I = \frac{K_I}{\sqrt{2\pi r}} f_{1ij}^I(\theta) + \frac{K_{II}}{\sqrt{2\pi r}} f_{1ij}^{II}(\theta) + \frac{K_{III}}{\sqrt{2\pi r}} f_{1ij}^{III}(\theta) \quad (1.24)$$

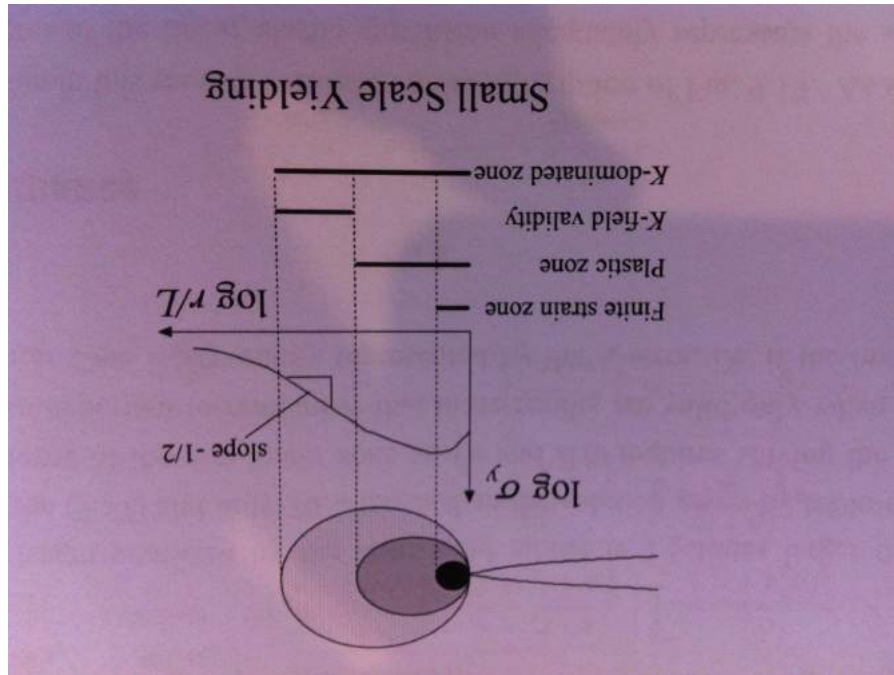


Figure 1.9: Scheme summarizing the different areas surrounding the crack tip. If the plastic zone becomes too large, it can overcome the k-dominance zone and reduce the K-field validity area to zero. In this case, linear elastic fracture mechanics is not valid anymore. [21]

Then, in this case it has been demonstrated that:

$$G = \frac{1}{E^*} \left( K_I^2 + K_{II}^2 + \frac{K_{III}^2}{1-\nu} \right) \quad (1.25)$$

These are simple assumptions but allow to understand how a fracture propagates through the material. However, in case of a too large plasticity zone, non linear fracture mechanics is applied. Then we can redefine G:

$$J = \int \left( W_v n_x - n_i \sigma_{ij} \frac{\partial u_j}{\partial x} \right) \quad (1.26)$$

Were  $W_v$  is the deformation energy density. From J the crack opening displacement  $\delta$  at the tip of the crack can be computed if necessary [21].

### Fracture stability

The criterion for increasing infinitesimally the crack length is given by either  $G > G_{IC}$  or  $K > K_{IC}$ , where  $G_{IC}$  and  $K_{IC}$  are called respectively energy release rate and stress

intensity factor. If this condition is verified, the crack will propagate either in a stable or unstable way, whether the loading is strain or stress deformed [21].

## 1.4.2 Damage properties of interfaces

### 1.4.2.1 Interface between two solids

Many different types of interfaces exist and can be defined as a border area between two dissimilar materials. The "material" term has to be considered strictly speaking, as it could be two identical materials but with different crystal orientations [23]. This section focuses on solid-solid interfaces, for which the interface separates two different solids. Many profiles are found for such interfaces, as illustrated in Figure 1.10, depending on many parameters such as the physicochemical interactions between the two solids [23]. This profile implies a given thickness for the interface, among which the chemical composition varies from the first material to the second. An

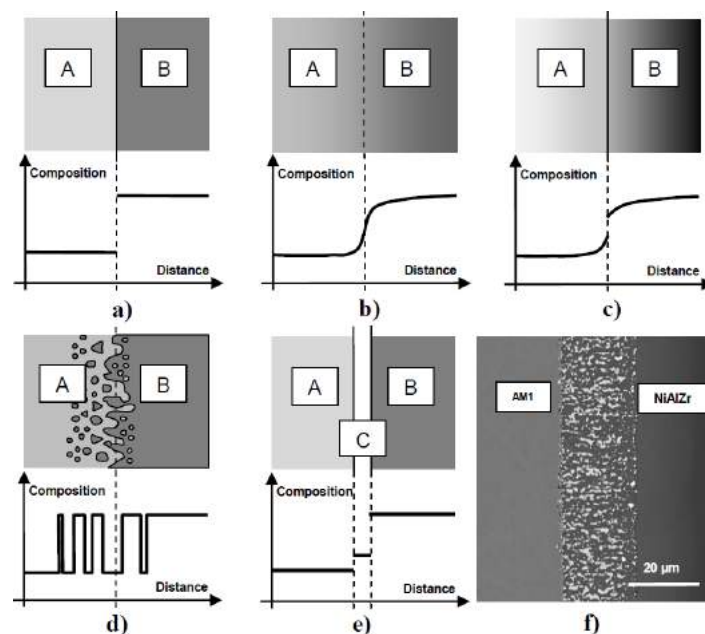


Figure 1.10: Schemes of different morphological profiles with their respective chemical composition as a function of the distance. The image f is a real profile illustrating the scheme (e) [23]

abrupt interface may be considered in order to facilitate the computation of the properties at the interface.

#### 1.4.2.2 Stress field in the case of a solid solid interface

For a solid solid interface, with a crack between two half planes of two different materials, the William expansion replaces equation 1.21 previously showed for a crack within a single material [23]:

$$\sigma(r, \theta) = \sum_{n=0}^{\infty} r^{\lambda(n)} F(\theta) \quad (1.27)$$

where  $\lambda$  is a complex value given by:

$$\lambda = n - \frac{1}{2} + i\epsilon \quad (1.28)$$

Equation 1.27 seems more complicated than equation 1.21 but shows similarities with the previous development, such as the singularity for values close to  $r = 0$ , even though the one here is oscillating [23].

#### 1.4.2.3 Adherence of the interface

The following expression describes the energy required to separate the two solids in order to overcome  $G_C$ , which is a combination of two terms [23].

$$G_C = \Gamma_0 + \Gamma_p \quad (1.29)$$

##### **Description of $\Gamma_0$**

On one hand, there is the energy required for the fracture mechanism (which includes the energy required to break bonds)  $\Gamma_0$ . It can be associated to the resistance of the interface  $\sigma_C$  corresponding to the maximum undergoing stress at the interface of the material which is loaded.  $\sigma_C$  can be computed through stress/crack displacement curves as it is showed in Figure 1.11 [23]. Two interfaces possessing the same value of  $\Gamma_0$  can thus lead to different adhesions. This difference comes from different values of  $\sigma_C$ , as shown figure 1.12 [23].

##### **Description of $\Gamma_p$**

On the other hand, there is the energy that can be dissipated by dissipation mechanisms occurring around the crack tip  $\Gamma_p$ , among the interface thickness and the two solids. The main energy dissipative mechanisms are plastic deformation and crack deflection [23].

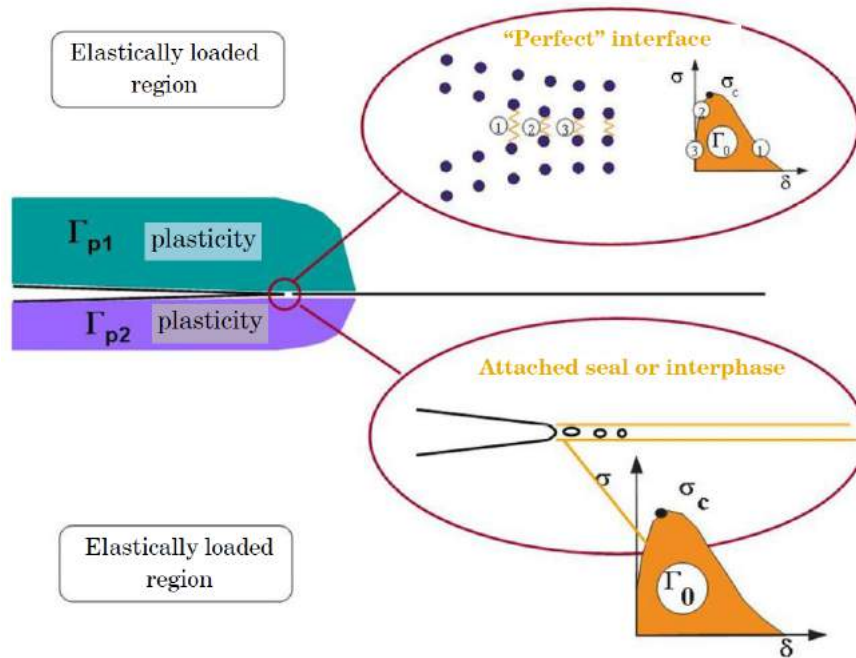


Figure 1.11: Scheme of a crack at the interface between two different materials. The energy of dissipation  $\Gamma_p$  is useful to compute the plastic deformation in the area in which plasticity occurs, in purple and green. The crack propagates for a stress higher than  $\sigma_c$ , the resistance of the interface. The energy of adhesion  $\Gamma_0$  is the area delimited by the stress/strain curve, where  $\sigma$  comes from an external force, and  $\delta$  is the opening of the crack. [23]

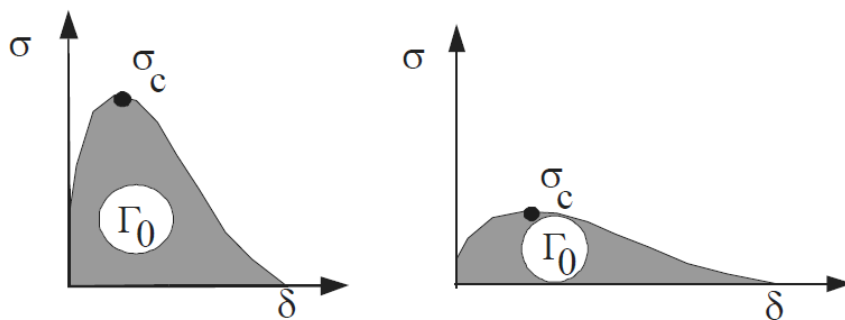


Figure 1.12:  $\sigma_c$  as a function of  $\delta$  for two interfaces having the same adhesive energy  $\Gamma_0$ . It shows that despite the same value of  $\Gamma_0$ , the values of  $\sigma_c$  can be different, leading to two different adherences [23].

Plastic deformation is a permanent deformation, by opposition to the elastic deformation for which the material comes back to its original configuration after unloading. It occurs for a stress called yield strength,  $\sigma_y$ . This stress is dependent on the material

itself, but also on its history, since its value can increase with plastic deformation [23].

Crack kinking, as well as deviation, among others, are one of the main dissipative mechanisms with plastic deformation. Crack deflection is really dependent on the configuration of the problem, namely on the external load, crack orientation, crack length and the heterogeneities. Figure 1.13 shows schemes of different interactions between a crack and an interface, and a real case of crack deviation from mode I to mode II due to an interfacial propagation [23]. Promoting these mechanisms

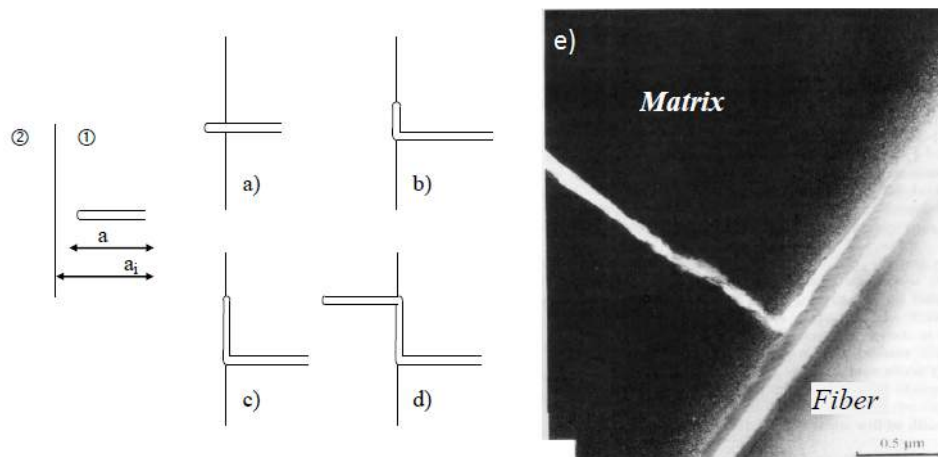


Figure 1.13: Left : The different interaction mechanisms between a crack and an interface. Right : Example of a crack deviation schematically illustrated by (b)[23]

demonstrated an increase of the interface resistance. This is why it is necessary to couple the fracture mechanism to the physico-chemistry of the interphases.

### $\Gamma_0$ and $\Gamma_p$ relationship

Despite the difference between  $\Gamma_0$  and  $\Gamma_p$  in term of contribution to  $G_C$ , these two terms are closely related and the associated phenomenon cannot be studied apart from each other. Indeed,  $\Gamma_p$  is directly dependent on  $\Gamma_0$  since for a higher ability to resist the crack opening, there is a higher ability to dissipate energy through dissipative mechanisms. Also, if the interface is weak enough, that is to say the interface breaks before the stress (von mise for instance) reaches the yield strength, plastic deformation does not occur and then  $G_C = \Gamma_0$ . On the other hand, if the interface can stand a load leading to a stress higher than  $\sigma_y$ , the term  $\Gamma_p$  appear and thus have a high leverage over  $G_C$  [23].

#### 1.4.2.4 Abrupt interface vs gradual interface

The hypothesis of a single interface is not realistic at the scale of the crack propagation, especially in the case of a morphological gradient. More accurate models exist. For example, a diffuse interface was modelled by a third intermediate layer between the two dissimilar materials, with a crack propagating at the interface of this added third layer and one of the 2 materials as showed in Figure 1.14 [24]. The added interface possesses varying properties, from ones of the first material to the ones of the second material, namely the elastic modulus. This type of model should be more accurate, especially for numerical simulations.

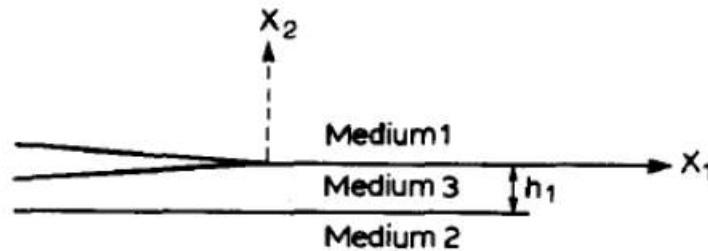


Figure 1.14:  $\sigma_C$  as a function of  $\delta$  for two interfaces having the same adhesive energy  $\Gamma_0$ . It shows that despite the same value of  $\Gamma_0$ , the values of  $\sigma_C$  can be different, leading to two different adherences [24].

To conclude, the analysis of fracture mechanisms in an homogeneous media gave the keys to properly analyse the damaging of solid-solid interphases. The adherence of a interface rules its resistance to damages. Finally, we saw some mechanisms allowing the dissipation of energy, and so the increasing of the fracture resistance. Knowing the existence of such mechanisms, we can play on the physico-chemistry of the interface in order to optimize its fracture resistance.

## 1.5 Physico chemistry and damage properties of TS-TP interphases

Cocuring the thermoplastic with the thermoset leads to specific interfaces, which possess many properties. The interphases come from the interdiffusion of the TP and the curing resin, due to the mobility of the chains. On one hand, thermodynamic equilibrium rules the mobility of the TS reactive species that tend to spread over areas of lower concentration, namely through the thermoplastic. On the other hand,

the resin penetration into the thermoplastic layer induce swelling and act against the diffusion process [7]. The balance between the two phenomena leads to a given thickness of the interface.

It is necessary to define the microstructure with two different scales. The smallest scale is the atomic one, at which interfacial energy rules the adhesion, as well as entanglements and covalent bonds. The interface at this scale delimits structures that are defined at a bigger scale, such as nodules and interpenetrating networks.

The second scale is larger as it is associated to the gradient of concentration and to the corresponding morphological gradient. The formation of this morphological gradient is due to both thermodynamics and kinetics. Indeed, there is interdiffusion of the thermoplastic and the thermoset monomers. Upon curing, reticulation increases the molecular weight of the thermoset chains, and decreases their ability to diffuse, so that the concentration profiles is determined by the varying ability properties of the thermoset. It also generates, as the molecular weight increases, demixion/phase separation. This creates a gradient of morphology finally depending on the phase diagram, the mechanism of phase separation and swelling. One can generally distinguish two different morphologies in the interdiffused zone of TP-TS interphases:

- In regions of high TS content, a few thermoplastic chains are dissolved in the TS at the early stages of the curing. At phase separation, these thermoplastic chains nucleate into small spherical domains, spreading all over the thermoset matrix. This structure is usually reported as a sea-island morphology. The average size of the nodules is essentially determined by the gelation time as it stops coalescence.
- At phase inversion, i.e. at relatively low thermoset contents the TS reactive species agglomerate into spherical cells close to each other and in equilibrium in TP matrix. This equilibrated, cellular structure appears when viscoelastic effects are significant. This is the case when dealing with a high T<sub>g</sub> thermoplastic. Using a low T<sub>g</sub> TP would most likely lead to another sea-island morphology as defined previously, giving rise to a symmetrical morphological gradient.

In between, located in the region of the initial interface, an inter-penetrating network might form under certain conditions, as illustrated by the work of Lestriez, in Figure 1.15 [25]. Such inter-penetrating network occurs for a given range of concentration. If this range is narrowed, the concentration gradient need to be small in order to spread

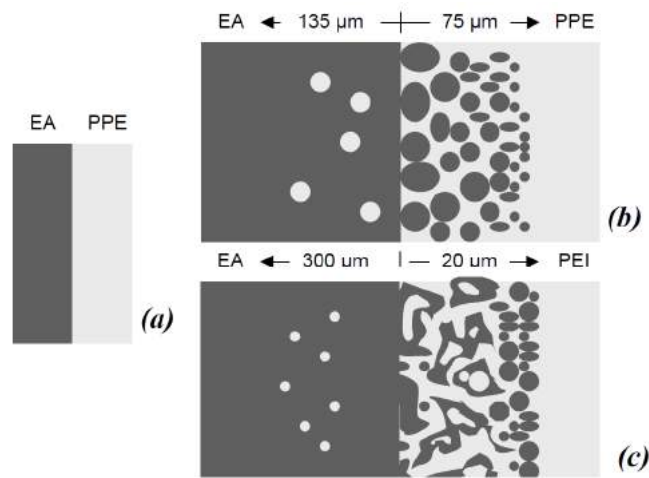


Figure 1.15: Scheme of the interphase morphologies formed by the curing of an epoxy resin on top of a TP film. On the bottom image one can observe a co-continuous phase as well as a sea island morphology (dark area) and a cellular morphology (black dots in the grey matrix)[25]

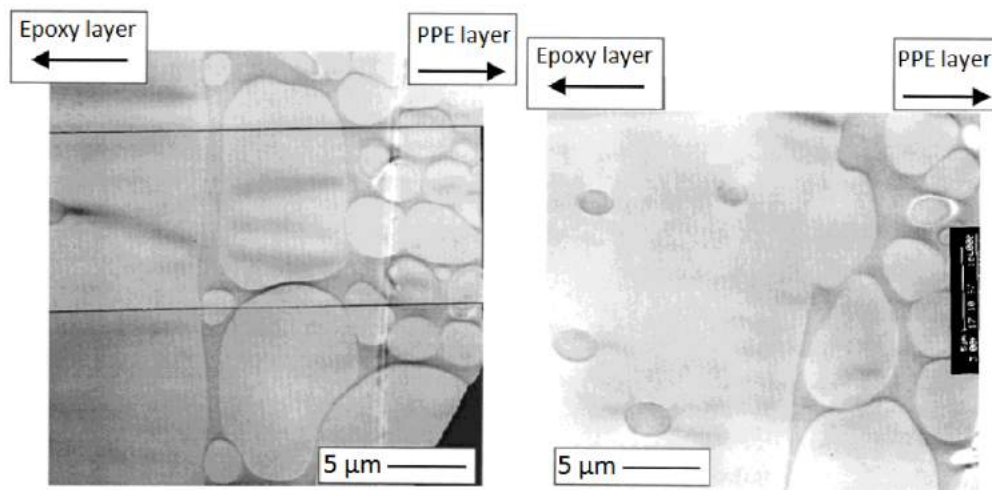


Figure 1.16: TEM clichés of a DGEBA-MCDEA (epoxy resins)/PPE (thermoplastic) interphase at either low (left) and high (right) conversion of the resin [7]

the limits of this concentration range far from each other. Also, the diffusion kinetics must remain low compared to the curing kinetics : a high viscosity prevents the phase separation to occur too fast compared to curing. If the concentration gradient is too high, one obtains an abrupt interface. If the viscosity of the mixture is too low, phase separation will proceed too far, forming a dual phase morphology one or the other condition is not fulfilled, it can lead to the only two morphologies described before

abruptly separated, as illustrated in Figure 1.15

According to some research, the presence of an inter-penetrating network is the key to an increased resistance to damage of the interface. Indeed, it tends to increase the resistance to crack propagation, mainly due to a better mechanical interlocking. It adds features for the fracture mechanism as it was described section (section of damage of interfaces). This resistance also increases with an increasing thickness of the interdiffusion area, and this was observed in thermoplastic/thermoplastic interfaces and, for our concern, in TP-TS interphases aswell [26].

To conclude, the choice of TP-TS couple as well as parameters lead to different morphologies, themselves leading to different fracture mechanisms. Privilegiating the formation interpenetrating network as well cellular morphologies is a key in the increase of fracture resistance. of the interphase.

## 2 Methods and Experiments

### 2.1 Materials

#### 2.1.1 RTM6 epoxy resin properties

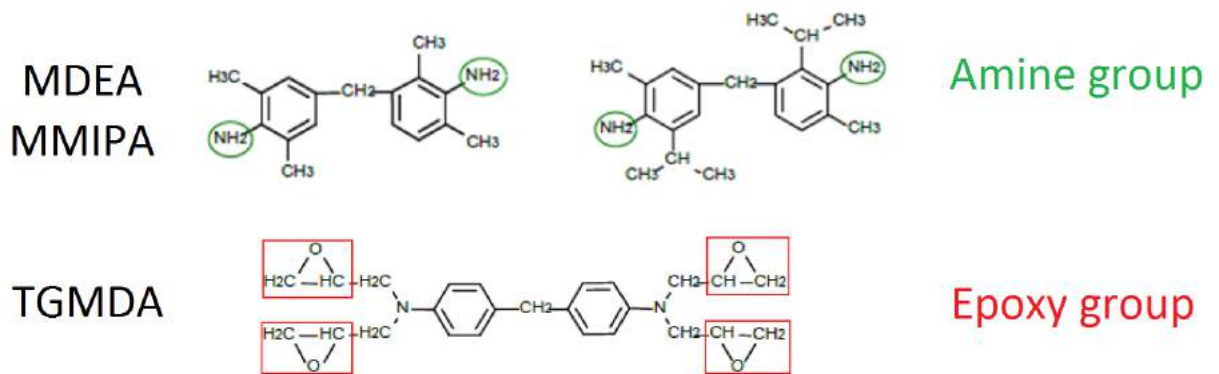


Figure 2.1: Diamine hardeners (top) and multifunctional epoxyde (bottom) forming the RTM6 resin synthesized by Hexcel.

The HexFlow(r) RTM6 thermoset resin is designed for the RTM process [27] and was used as the thermoset polymer for the samples prepared during this master thesis. The resin is a pre-blended epoxy-amine mixture made of three different tetrafunctional monomers: the epoxyde molecule Tetraglycidyl Methylene Dianiline (TGMDA) and the amine molecules 4,4'-methylenebis(2,6-diethylaniline) (MDEA) and 4,4'-methylenebis(2-isopropyl-6-methylaniline) (MMIPA), seen in Figure 2.1. It also includes additional particles providing extinguishing properties against fire [28]. The uncured RTM6 Tg is -15°C and the cured RTM6 Tg is 220°C. TGMDA will react following the reaction showed in Figure 2.2 with the diamines and form a 3D network due to the functionality the reactive species,

#### 2.1.2 PEI

Polyetherimide (PEI) is a high performances amorphous polymer with high thermal resistance and good mechanical properties. The PEI used for this master thesis polymer is showed in Figure. 2.3, the PEI Ultem 1000 synthesized by Sabic. Its glass transition temperature Tg is around 220°C. The high thermic resistance is due to the

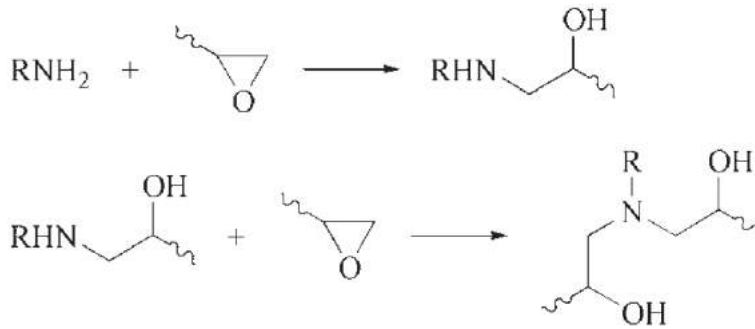


Figure 2.2: Reaction mechanism occurring during the epoxy resin reticulation: the amine group first react with the epoxy group [29]

functional group imide, but unlike the family of polyimides, the ester bond makes the polymer chains less rigid and so less viscous.

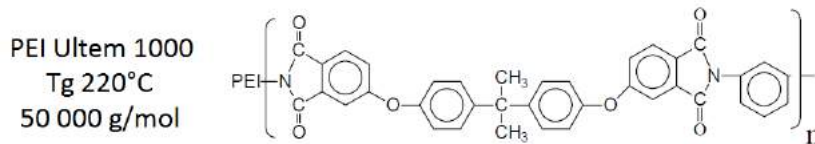


Figure 2.3: Polyetherimide PEI structure of PEI Ultem 1000 synthesized by Sabic. Drawing from [7]

### 2.1.3 PETT

PETT is a thermoplastic and an amorphous version of poly(ethylene terephthalate), commercially denominated t-glass and provided by Taulmann 3D [30]. It is easily differentiable from the other polymers used in the 3D printer such ABS and PLA due to its transparency. PETT has a low Tg around 80°C. This polymer derives from the poly(ethylene terephthalate)

## 2.2 Preparation

### 2.2.1 RTM6 - curing procedure

The temperature cycle for the curing of the RTM6 used is the following one, see Figure 2.4:

- Temperature ramp from room temperature (RT) to 90°C

- Isotherm at 90°C for 20 minutes, the time for the resin to be at 90°C
- Temperature rampe from 90°C to 160°C with a slope of 2 per minute
- Isotherm at 160°C for 90 minutes
- Temperature ramp from 160°C to 180°C with a slope of 2 per minute
- Isotherm at 180°C for 120 minutes
- Temperature ramp down to room temperature naturally

The following formula was considered to simulate the conversion curve associated to this temperature cycle [16]:

$$\mathcal{R} \equiv \frac{\partial \xi}{\partial t} = \left( \frac{k_1 k_d}{k_1 + k_d} + \frac{k_2 k_d}{k_2 + k_d} \xi^e \right) (1 - \xi)^f$$

$$k_{1,2} = A_{1,2} \exp\left(-\frac{E_{1,2}}{RT}\right)$$

$$k_d = A_d \exp\left(-\frac{E_d}{RT}\right) \exp\left(-\frac{1}{f_1 T - f_2 \xi / (1 - f_3 \xi) + f_4}\right)$$

where R is the gaz constant, T the temperature,  $\epsilon$  the conversion of the resin, e and f the partial orders of reaction,  $E_1$ ,  $E_2$  and  $E_d$ , are the activation energies, and  $A_1$ ,  $A_2$ ,  $A_d$ ,  $f_1$ ,  $f_2$ ,  $f_3$  and  $f_4$  are constants, defined by:

$A_1$	$2,10^6 \text{ min}^{-1}$	$f_1$	$3 * 6,96.10^{-3} \text{ K}^{-1}$
$A_2$	$3,69.10^5 \text{ min}^{-1}$	$f_2$	0,831
$A_d$	$6,39.10^6 \text{ min}^{-1}$	$f_3$	0,506
$E_1$	$7,32.10^4 \text{ J.mol}^{-1}$	$f_4$	0,381
$E_2$	$5,25.10^4 \text{ J.mol}^{-1}$	$e$	1,25
$E_d$	$5,04.10^4 \text{ J.mol}^{-1}$	$f$	1,54

The RTM6 can be pre-cured to a certain extent of conversion before cocuring with the thermoplastic layer. It gives the ability to control the diffusion kinetic by tunic the viscosity of the thermoset at the fist contact with the thermoplastic. To do so, the gel time is an important property of the resin to know : it is the time for a given temperature cycle at which the resin starts forming a three dimensional network. Table 2.1 shows some of the gelation times of the RTM6 for different isotherms from 120°C to 240°C [27].

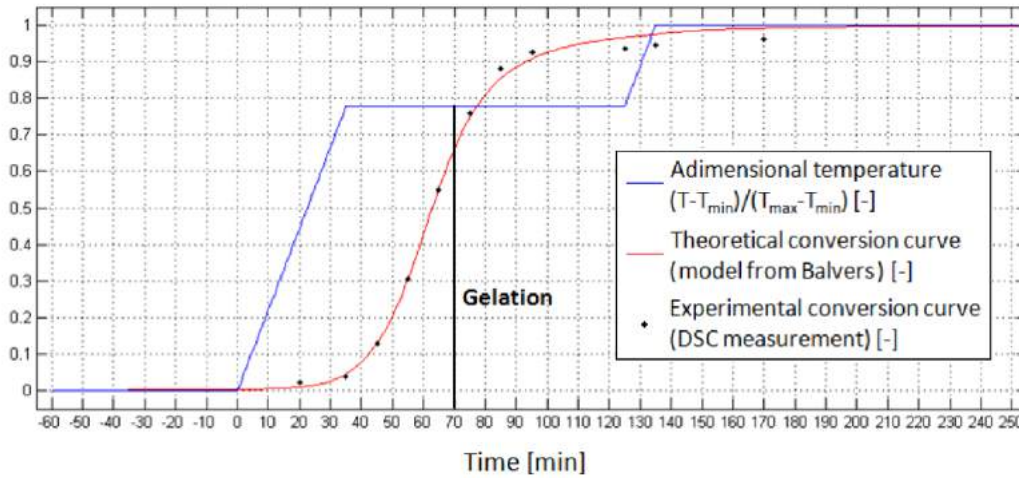


Figure 2.4: Curing cycle used, with the corresponding simulated and real conversion of the thermoset resin [16]

Temperature (°C)	Time (min)
120	>240
140	95
180	30

Table 2.1: RTM6 gelling time as a function of the curing temperature

## 2.2.2 Polymer blends

In order to obtain the best initial homogeneity, polymer blends were prepared by dissolution with a solvent. Blends of RTM6/PEI and RTM6/PETT were prepared via dissolution into dichloromethane. The following procedure was followed:

- rest of the resin at room temperature normally stored at  $-19^{\circ}\text{C}$ ,
- thermoplastic dissolution into dichloromethane until no particles are visible, in a becher,
- adding of the resin to the solvent containing the thermoplastic
- solvant natural evaporation while agitated with a magnetic agitator during a whole night,
- degasing in a furnace connected to a pump, at  $90^{\circ}\text{C}$ . Keeping the agitator helps the bubble nucleation, and
- pouring in a mold and curing cycle.

It was more convenient to degas directly from the becher considering the large surface of the sample. However, some samples showed a high viscosity such that either degassing was impossible due to stuck bubbles or pouring in the mold was impossible. An other process was carried out in this case:

- Pouring was done before degassing and degassing was proceeded directly into the mold
- degassing was proceeded at higher temperature, up to 140C, despite the fact that the curing reaction is already quite active at this temperature. We managed to end the degassing before the crosslinking %age reached 10 %, far from the gel.

Depending on the required shape, the solution was poured into the corresponding mold, and machining of the cured samples was performed to obtain the required dimensions, for SENB tests and compression tests.

### **2.2.3 Press: thin films**

#### **PETT thin films**

Thin films of PETT were prepared with a press. Initially stored in coils with a 1.75mm thin in diameter filament, films were pressed at 180C under a maximum load of 10 kN. In order to avoid any remaining stress among the thin film, after each pressing, the film rested on a plate at 180C and then cooled down in air in order to relax stresses among the film. It reduces its deformation during the curing cycle for which the temperature does not exceed 180C. This whole step was repeated as long as the film thickness did not reach the required thickness at +-10 %, namely 300 microns.

### **2.2.4 Laser patterning**

#### **Description**

In order to pattern the PEI surface, etching by laser was performed. The laser used was the Laser-as-2 with a power of 2 watts, affordable for 200 euros. The software librecad was used to define the 2D pattern and the interface Arduino, an Open-source electronic platform, was in charge to convert the pattern drawn on librecad into a path that the laser must follow. This path consists in a succession of dots, spaced

from each other from a minimum distance, that the laser beams in order to etch the surface. The interface gives access to a range of different parameters such as the image-real pattern ratio.

### **Achievable smallest feature printed**

The conversion of the drawn pattern into a path for the laser lead to a path that follows the border of the path, as described in Figure 4.2 with the red dots : it is not possible to make the laser draw a single line of dots since the line, as thin as it could be, is seen by the laser as a rectangle. This condition gives the theoretical smallest feature achievable, which is two times the width of a dot plus the space in between, namely around 20 microns . However, assuming this scale is reachable, it requires an accurate setting of the parameters

### **2.2.5 3D printing patterning**

The 3D printer Markerbot Replicator x2 was used to print PETT films with a given roughness. This 3D printer uses the fuel deposition modeling, see Figure 2.5 [31]. A filament of polymer is led to the extruder mechanically, with an accurate control on the quantity sent to it. This extruder follows a heater block that heats the filament at a high enough temperature to melt it. Also, a great control of temperature is required since the viscosity, an important parameter, depends on the temperature. A variation of 10 degrees from an operational setting can lead to failures, or printing can also be impossible. The melted filament goes through the extruder's nozzle under pressure: the nozzle size is smaller than the initial diameter of the filament. Finally, the sample is printed layer by layer [31].

The main features of the Markerbot Replicator 2x are:

- Resolution: 100 microns over x, y and z axis
- Nozzle diameter: 0.4 mm. The nozzle imposes the X-Y resolution. However, this smallest resolution can go under 400 microns.
- Resolution of 100 microns in the z axis direction
- For our experiments, the plate on which printing is performed is coated with a film of polyimide, allowing a better sticking of the sample to the plate.

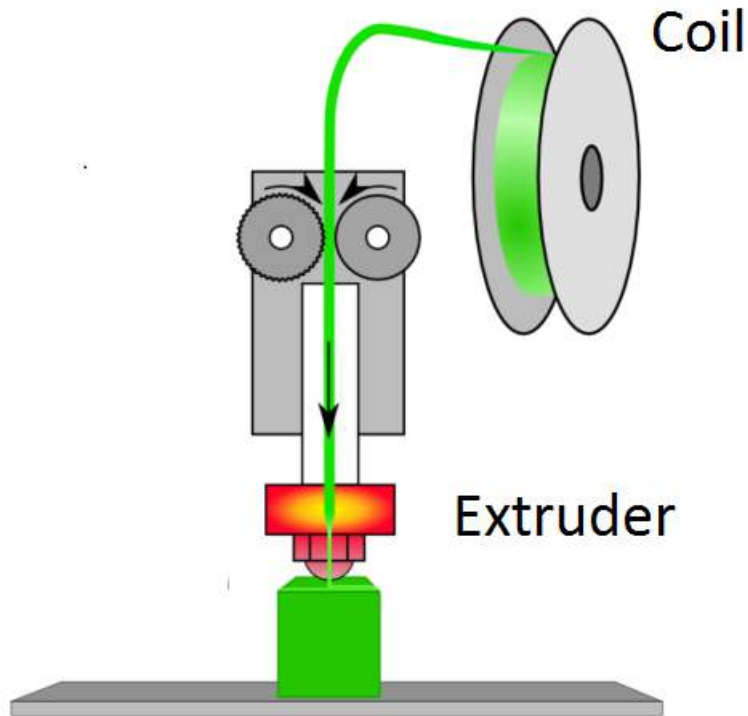


Figure 2.5: Scheme of 3D printer for Fuel Deposition Modeling. The polymer, green in this scheme is brought to the extruder, heated and deposited, forming layer by layer the sample. [31]

The advised parameters for PETT 3D printing are [30]:

- Extruder temperature from 230°C to 248°C
- Slow printing speed, namely 50 mm/s instead of 150 mm/s for ABS and PLA printing materials commonly used in FDM.

According to the length of inter-diffusion of the PEI and PETT with the RTM6, patterned films of PETT were printed with a size of the smaller dimension neighbouring 100 $\mu$ m. One can see in Figure 2.6 a side cut of such a patterned PETT thin film printed. The size of the samples prepared with the 3D printer, approaches the resolution limit: a rigorous printer setting was done before every utilization. Before each batch of experiments, the levelling of the building plate as well as the loading of the sample were done. During loading, we made sure no residual polymer from the previous uses was still in the extruder, by keeping loading the PETT filament for a few seconds.

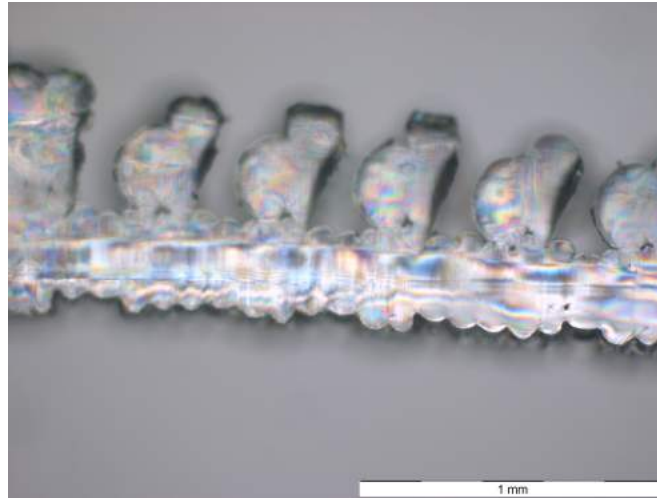


Figure 2.6: Image of the sidecut of a 3D printed PETT film. The film was printed vertically, and the plan on which the sample was supported during upon printing is the plan XY. The layers are seen circled in red, and show the resolution limit of the 3D printer configured at the smallest scale possible. One can observe the round area formed by the tip under each crenel: this can be improved by using the printer printing 2 materials at the same time, the second one being a sacrificial bridge removed after the printing.

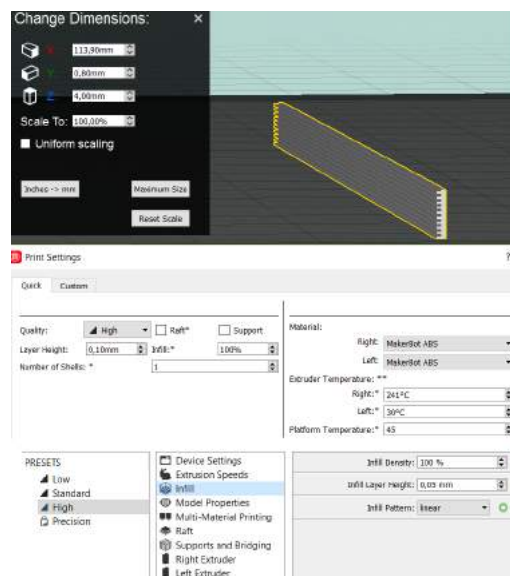


Figure 2.7: Picture of the software used for the 3D printing : it shows here the parameters used for the printing of the film showed in Figure 2.6. It is a short view of the possible parameters available to tune the printing

### 2.2.6 Interphases

**Interphase samples for physico-chemical characterization.**

Samples for the physico-chemical characterization were prepared following the procedure:

- Aluminium cylinders of dimensions were cleaned in acetone bath.
- After the thin film preparation (see 2.2.3), the thin films were heated up to 180C in order for the film to be deformable (above Tg).
- Aluminium cylinders were manually pressed on the thin film in order to push the cylinder into the film, without going through all the film.

### **Interphase samples for mechanical characterization.**

Samples of RTM6 containing films of thermoplastics where prepared with the following procedure:

- After the film preparation (see 3D printing or press), two polyimide films are placed on the film and maintained with tape. The polyimide films are placed in a way that they reach half of the sample (in height) prepared in the mold. The two polyimide films act as an artificial precrack at the interface for SENB tests.
- The prepared thin film with the polyimide stack is disposed into the mold. see the profile view Figure 2.8.
- After closing the mold, the epoxy resin is poured into it. The curing cycle used was the cycle described at the 2.2.1.
- Finally, after curing, the samples are demolded and machined for SENB tests.

### **2.2.7 Surface preparation by microtomy**

The surface preparation by microtome consists in preparing flat surfaces for the nano-indentation. A Cryo-ultra Reichert microtome was used, equipped with a Histo-Cryo diamond blade. Samples were first cut to show a surface small enough to fit the blade and to avoid its damaging.

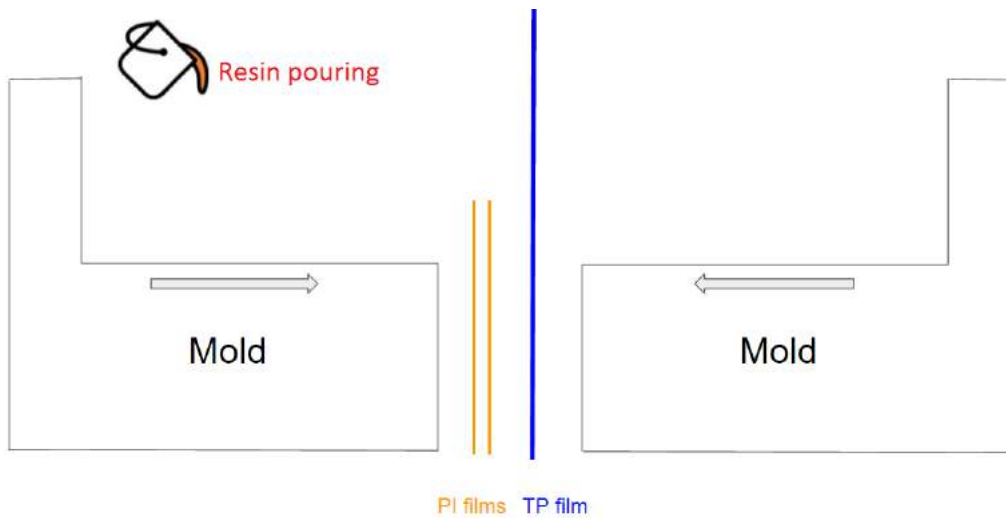


Figure 2.8: Scheme of the profile vue of the samples prepared for SENB preparation : the two polyimide thin films as well as the thermoplastic film are tightened by the mold. Then the resin is poured in the blank spaces A. The arrows indicte that all the layers and the mold are sticked and tightened by the mold

## 2.3 Characterization

### 2.3.1 Physico-chemical characterization

#### Differential Scanning Calorimetry (DSC)

DSC, which stands for differential scanning calorimetry, is a method that allows to

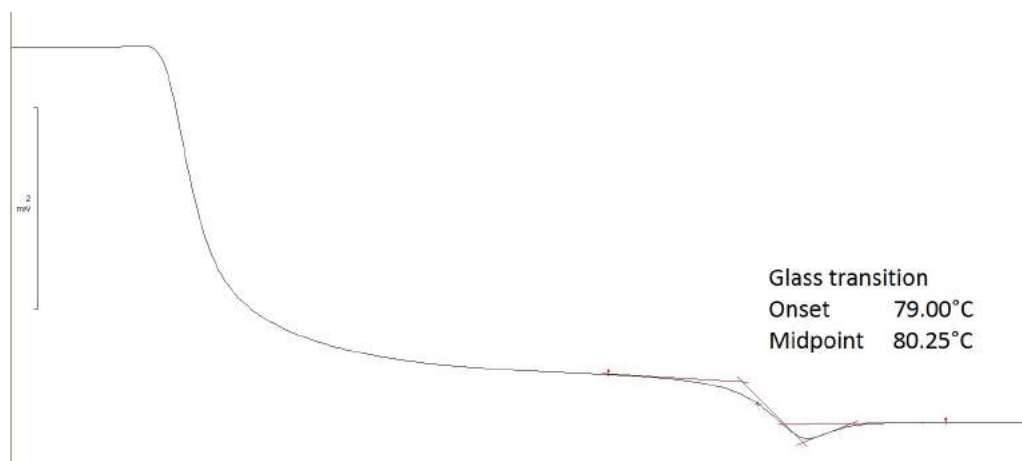


Figure 2.9: DSC curve of a PETT sample : it reveals its Tg around 80 °C, and no other transformations up to 300°C

detect a glass transition and/or crystallization/melting. It consists in heating both a reference and the measured sample. The equipment, via a retroactive loop, heats while maintaining the temperature equal in both the reference and the sample. When a transition occurs, for example an exothermic one, the equipment needs less power to provide to the sample to heat it at the same temperature than the reference. The equipment records the heat flow needed to increase the temperature with time, and detect for instance that it requires less energy to heat the sample during the transition. For our tests, the reference used was a sample of Indium with a mass of 9.93 mg.

### **Thermogravimetric Analysis (TGA)**

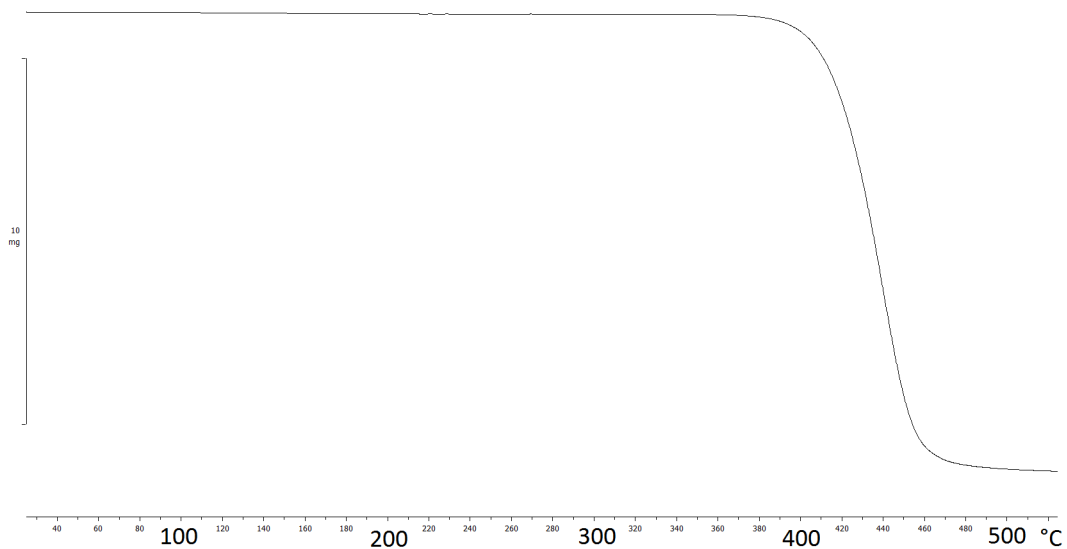


Figure 2.10: TGA analysis of a PETT sample, showing its degradation at 400°C

The TGA was used here to determine the PETT degradation temperature. It consists in measuring the mass of the sample while heating it : if any degradation of the polymer occurs, it will produce chemical compound in gas form and the sample lightens.

### **Microtome: optical microscope**

Microtome cuts of cured samples were prepared for optical microscope observations. To do so, a Cryo-ultra Reichert microtome was used, equipped with a Histo-Cryo diamond blade. Samples were first cut to show a surface small enough to fit the blade and to avoid its damaging. The blade possesses a micro tank containing water, the cut sample goes into the surface of the water and stays on it because of the surface tension. The sample is taken thanks to a tiny glass bubble slightly dipped into the

water. Because of some dysfunctional features with this machine, the thickness of microtome samples was regulated manually. However thanks to the color of the so cut layers (ie purple to green) we could determine a sample thickness between 200 and 400nm.

### **Optical microscope**

In order to characterize the samples, a fast and efficient method was performed. After their preparation (see Microtome), samples were deposited on a glass support, dried first by heating briefly with a heating plate, with a short enough time in order to avoid any sample degradation. For transmission observations, a droplet of oil was deposited and the observations were performed.

The observations were done with an TH4/200 Olympus optical microscope by phase contrast image, with the following (and successive) magnifications:

- x10, phase 1 observation
- x60, phase 3 observation
- x100, phase 3 observation

## **2.3.2 Mechanical characterization**

### **2.3.2.1 SENB**

SENB tests were performed in order to determine the fracture toughness of the inter-phases prepared. This test, standing for single edge notched beam, was proceeded under the ASTM-D5045 norm citenormsenb. This norm imposes samples with the shape showed in Figure 2.12. As it was explained in the state of the art, small scale yielding is required to perform tests with correct values. This condition is given by the formulas (Source???):

$$B > 2.5 \left( \frac{K_{IC}}{\sigma_y} \right)^2 \quad (2.1)$$

$$a > 2.5 \left( \frac{K_{IC}}{\sigma_y} \right)^2 \quad (2.2)$$

$$W - a > 2.5 \left( \frac{K_{IC}}{\sigma_y} \right)^2 \quad (2.3)$$

Where  $B$ ,  $a$  and  $W$ , showed in Figure 2.12 are respectively the thickness of the sample, the height of the sample, and the total length from the tip of the crack to the border of

the sample, in the direction of the crack propagation.  $K_{IC}$  and  $\sigma_y$  are, as defined in the state of the art), the stress intensity factor and the yield stress.

### **Crack initiation**

It is compulsory to make the crack start at the thermoplastic-thermoset interface. Indeed, we want to characterize the ability of such interface to resist any crack propagation. If the crack is too far away from the interface so that there is no interaction with the interface, the test would give the pure RTM6 properties, which is not the properties we are looking for. Moreover in case the thermoplastic thin film is patterned, it is advised to initiate the crack in the thermoplastic at the beginning of the patterning. To do so, instead of using a razor blade to initiate a pre-crack (that would also potentially break the sample while knocking it) the crack initiation was done by inserting thin films of PolyImide (PI) between the resin and the thermoplastic, before curing. This thin film acts as a separator and prevents the interdiffusion between the thermoplastic and the thermoset locally where the PI film is inserted. The thin film(s) was introduced in a way showed in Figure 2.8. The use of such crack initiator allows a good reproducibility. A double PI thin film was introduced when the thermoplastic used was PETT in case the film would stick to the thermoplastic, the crack being the interface between the double PI thin films and the thermoplastic.

### **Test**

The test is a three-point flexural test consisting in bending the SENB specimens in a way the crack open in mode II. The sample is inserted between 3 axes, 2 on one side, one on the other side. These axes are incorporated in a Zwick Z250 Roell machine loading at a constant crosshead displacement rate of 1 mm/min.

#### **2.3.2.2 Nano-indentation**

##### **Principle**

In order to extract the hardness of our samples, nanoindentation was used. A test consists in indenting the surface of the sample we want to analyse. Then the load displacement curve is recorded during the tip penetration into the sample. The tip used was a Berkovich tip, for which the load-depth relationship of the tip is given by :

$$h = \sqrt{P} \left[ (3\sqrt{3}H \tan^2 \theta)^{-\frac{1}{2}} + \frac{2\pi - 4}{\pi} \frac{\sqrt{H\pi}}{2\beta E^*} \right] \quad (2.4)$$

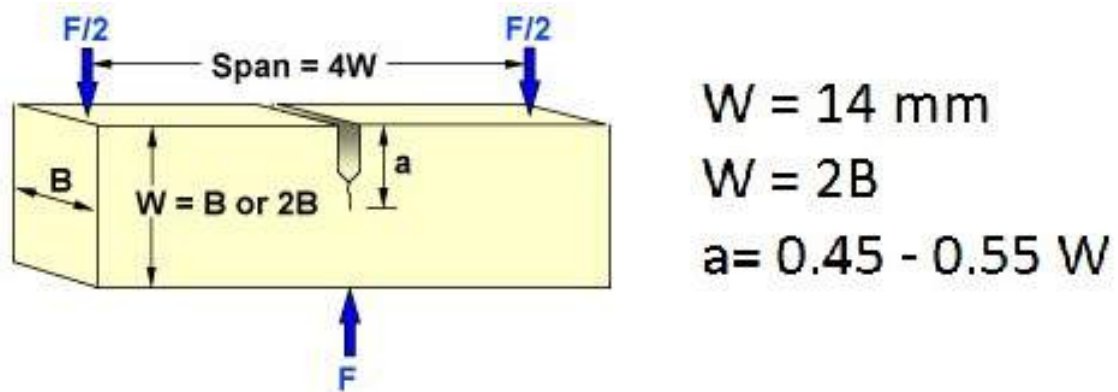


Figure 2.11: Scheme of the geometry of SENB samples imposed by ASTM-D5045 norm [32].

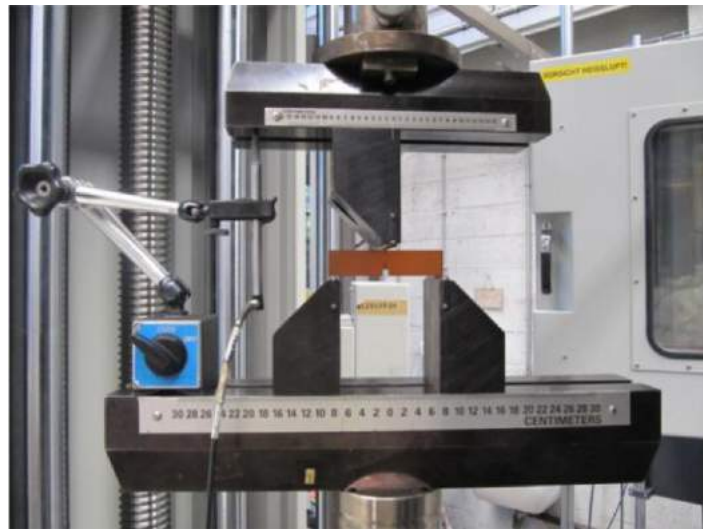


Figure 2.12: Experimental setup of the SENB test : the sample is between three beams, applying a force on it, such that the resulting test is a flexion test.

where  $H$  is the hardness given by  $H = \frac{P}{A}$ ,  $A$  the contact area,  $E^*$  the indentation modulus  $E^* = \frac{1}{2} \frac{\sqrt{\pi}}{\sqrt{A}} \frac{\partial P}{\partial h}$ .

where  $R$  and  $\theta$  are the combined radii and angle of the indenter and the shape of the residual impression in the specimen surface [3]. The computation of the results necessitates some assumptions such as elastoplasticity during loading, while plastic deformation is neglected during the unloading.

### Tests

The tests were performed on a Hysitron Triboscope mounted on a Park autoprobe

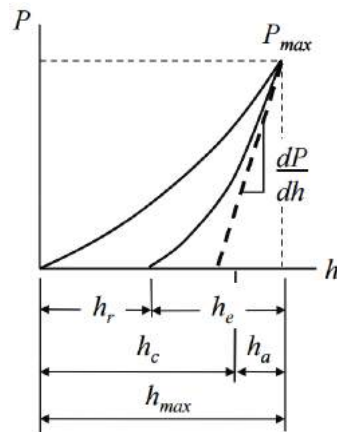


Figure 2.13: Load-unload plotting of  $P$  as a function of the penetration depth of the nano-indent

cp AFM-STM apparatus using a pyramidal Berkovich diamond indenter, with a tip modulus of  $1.1410 \cdot 10^6 \text{ MPa}$ . Because of the sensitivity of such tests, experiments were performed at constant temperature, namely 25 degrees. For each sample, 16 indents were performed, each indent separated from each other of at least 36  $\mu\text{m}$ , as illustrated in Figure 2.14 where a PEI plate has been indented. For prepared surfaces, indents were done forming a regular square containing 4x4 indents. Otherwise, indent location was manually selected.

### Compression tests

Uniaxial compression tests were carried out on a Zwick Z250 Roell machine under the norm ASTM-D695 [34]. The specimens are squared cylinders having both height and diameter equal to 10 mm. The testing procedure is the following one :

- cylinders are made according to the description of the section (aaa) with a mold leading to a bigger volume than the required cylinder
- the resulting sample is machined to fit the requirements of the sample geometry imposed
- the cylinder is placed in subpress to make sure that everything is aligned with the machine.
- The subpress is placed on the compression machine
- the cylinders are lubricated with a 70  $\mu\text{m}$  thick teflon film on each side in order

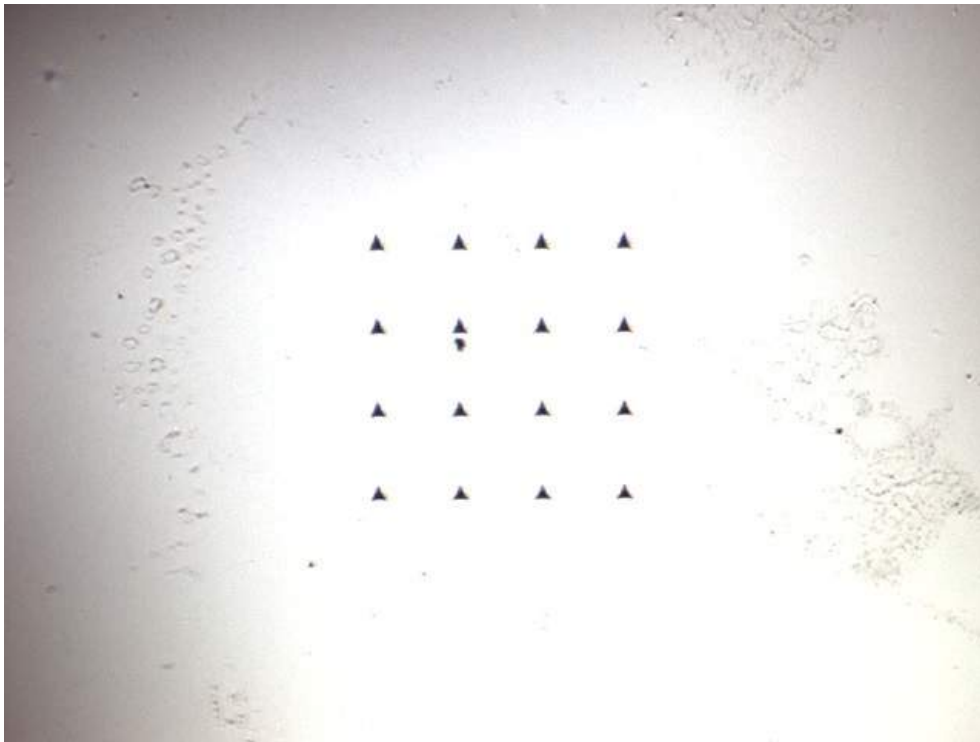


Figure 2.14: Indent pei

to avoid excessive friction of the cylinders with the machine, which can lead to barreling, as illustrated in figure 2.16.

- the compressive load was applied at constant crosshead displacement rate of 1, 10 or 100 mm/min.

The set up is illustrated in figure 2.15.



Figure 2.15: Experimental setup of the compressions tests.

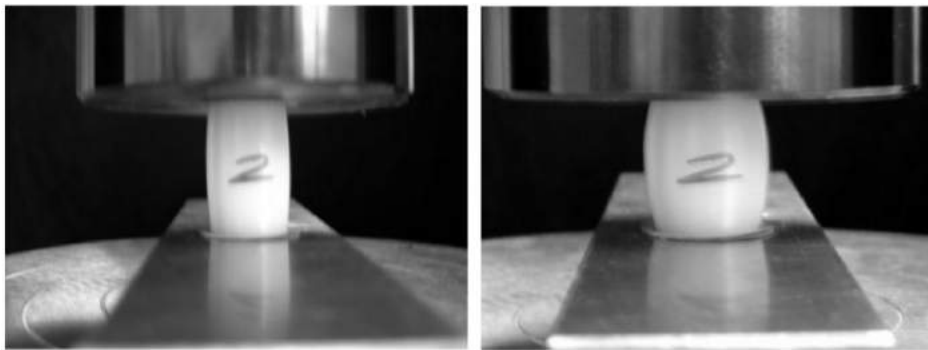


Figure 2.16: Illustration of the barreling effect

### 3 Study of plane interphases

---

The aim is to obtain co-continuous zone into the morphological gradient in order to toughen the interface by adding fracture mechanics features such as the ones described in the section of fracture mechanisms. It was already achieved with PEI following the curing cycle in the work of Quentin Voleppe [16]. This is why this study was performed with another polymer we could 3D print, namely PETT. Indeed, a TGA measurement, showed in Figure 2.10, shows that PETT does not degrade under 300°C,

while the curing temperature does not exceed 180C. First, PETT/RTM6 interfaces were prepared with initially flat PETT films, in order to:

- asses the feature size of the roughness regarding the RTM6/PETT interphase length of interdiffusion.
- compare the mechanical properties with the PETT/RTM6 interfaces with an initially rough PETT thin film.

### 3.1 Characterization of the interphases and discussion

#### Flat interphases characterization

PETT/RTM6 interphases with an initial flat PETT film and a precured resin were prepared for characterization accordingly to the procedure described. The choice of precuring the resin is that we expected the interdiffusion length to be too large since the PETT Tg is relatively low. Sample preparation remained the same but pouring was done at a certain time of the curing cycle corresponding to a percentage of reticulation, arbitrarily chosen at 30 % of conversion. Fig 3.1 obtained with an optical microscope shows the morphology gradient, with an interpenetrating polymer network.

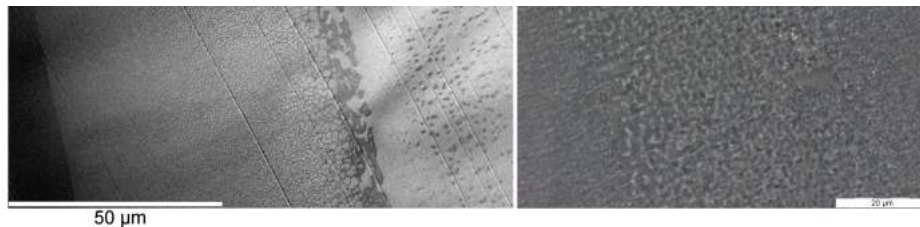


Figure 3.1: PETT-RTM6 and PEI RTM6 interfaces following the curing cycle described before. with an initially flat thermoplastic film

We can first observe a co-continuous area. The needed conditions required for the formation of an interpenetrating network are then fulfilled. It probably comes from the fact that :

- the PETT glass transition temperature is under the curing temperature by 100C. At this temperature, PETT is no longer in a glassy state. It implies a better mobility of the thermoplastic chains, and so a longer area on which the concentration gradient is spread

- at the same time, due to pre-curing, gelling time arrives fast so that the resin chain viscosity is drastically reduced. It allows a lower kinetic of phase separation, which does not reach equilibrium before gelling time.

Moreover, the sea island morphology is observed from either side of the cocontinuous domain. This differs from the morphology obtained with PEI, that showed on the TP rich phase a cellular morphology. There is a competition between the length of interdiffusion and the microstructure. Indeed, for good mechanical properties the best is to spread the diffusion length as far as possible. This is doable if the TP have a low  $T_g$ . On the other hand, the cellular structure contributes to toughening, and this morphology is observed for high values of  $T_g$ .

### **Length of interdiffusion**

Despite a well defined interpenetrating network, we could not optically distinguish any diffusion front as it was done for PEI/RTM6 interphases. In order to determine the length of interdiffusion, we could assess that the diffusion process is linear, following a Fickian model. Indeed, the PETT is 100 degrees above its glass transition temperature. Raman spectroscopy, chemical treatment or SEM were not performed. However, polymer blends with different concentrations of thermoplastic were prepared in order to determine the concentration for a given morphology, and apply the obtained results to compute the length of interdiffusion. To do so, we looked at the areas of the interphase corresponding to the structures we obtain with homogeneous blend, and attribute at this area the corresponding percentage of thermoplastic of the homogeneous blend. It was assumed that with PETT the total interdiffusion length is about 250 microns on figure 3.3. However, this result is not precise since it was determined by a subjective method.

However, despite the non-preciseness it confirms the fact that the interdiffusion length is too large.

### **Control of the interdiffusion length by pre-curing**

Given the assumed size of the interdiffusion length, there is a need to reduce it for the following reasons:

- a too large diffusion length implies to increase the feature size, that would have led to a too large thin film and too large roughness
- interdiffusion lengths must remain close from the results obtained with PEI in

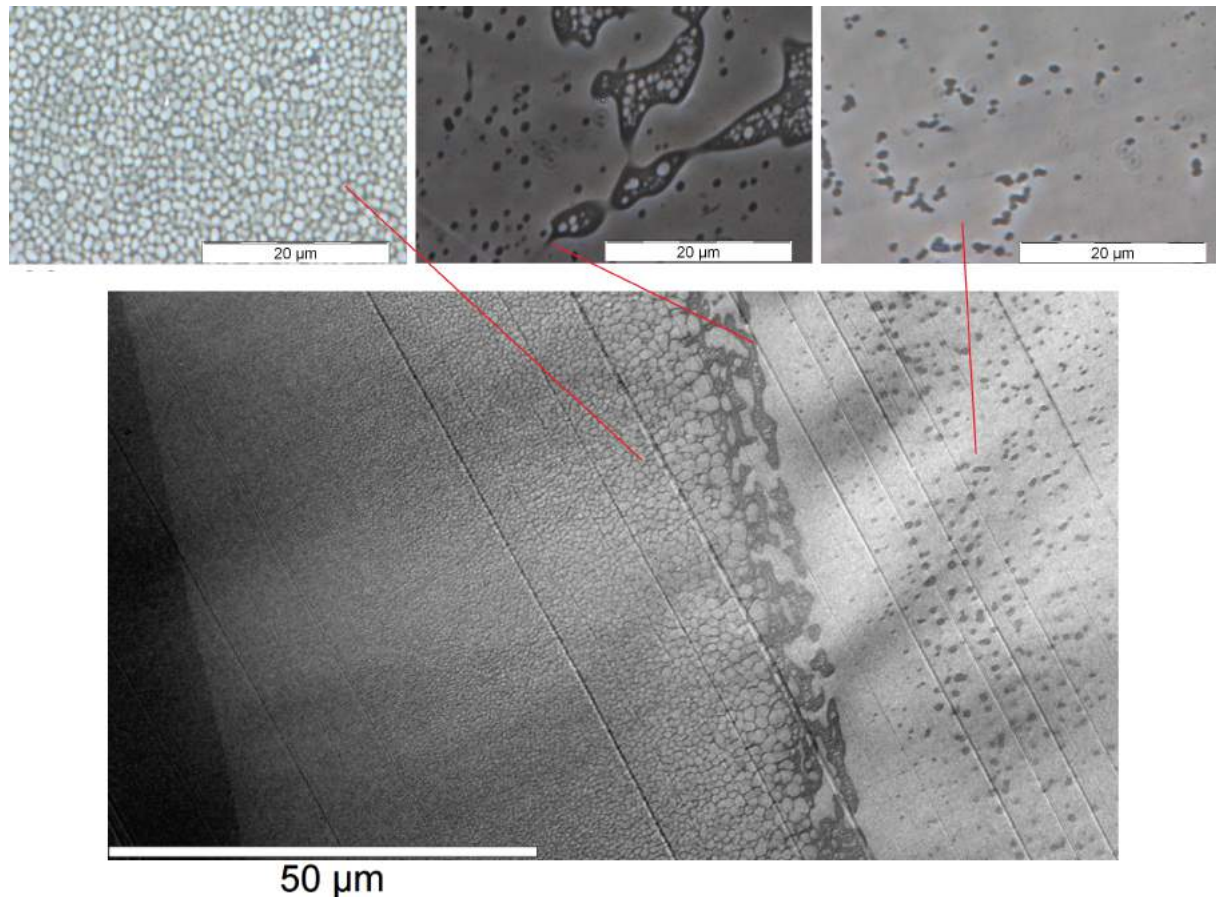


Figure 3.2: Optical images of PEI/RTM6 cured homogeneous blends. The top three images are the observed morphologies of the respective concentrations of 5, 15 and 25 weight % in PEI, that can be identified (arrows) in the morphology gradient of the PEI/RTM6 interphase.

order to properly compare them. Indeed, we cannot proceed to comparisons if the thickness varies from a sample to each other, since its a crucial parameter in the resulting resistance to the crack propagation.

A diffusion length control was achieved by pre-reticulating the resin before pouring the resin in contact with the thermoplastic film. Indeed, a pre-reticulated resin have chains with a higher molecular mass than the monomers, leading to a weaker length of diffusion compared to the initially non reticulated monomers of the RTM6. It was possible to determine the reticulation percentage as a function of the time of curing following the Figure 2.4. Table 3.1 list the samples prepared this way :

Fig 3.4 shows how the interpenetrating polymer network have been reduced down to microns for the sample with a precuring of 50 % conversion.

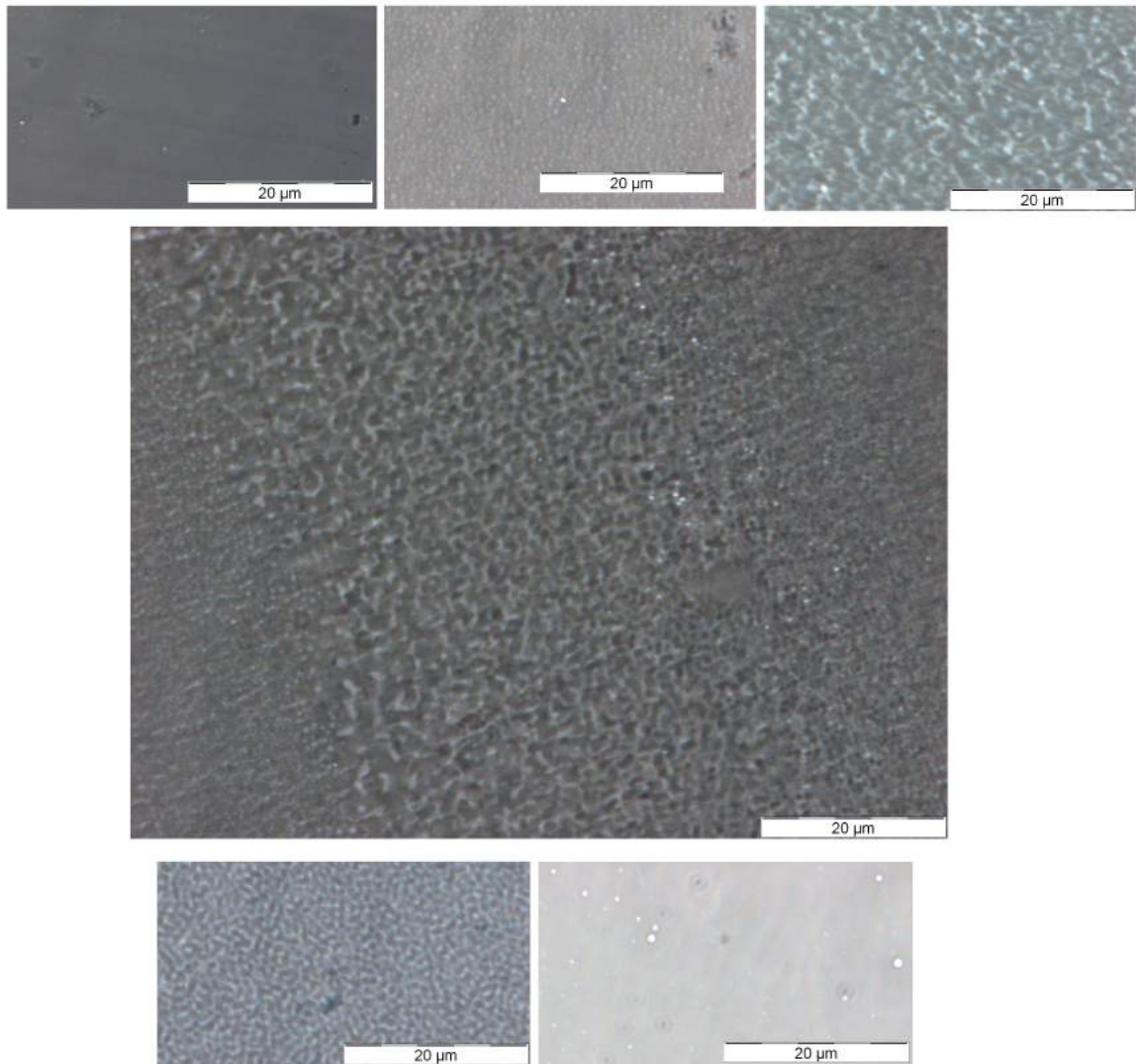


Figure 3.3: Optical images of PETT/RTM6 cured homogeneous blends. The top images are the observed morphologies of the respective concentrations of 5, 15 and 20 weight % in PETT. The bottom images are the observed morphologies of the respective concentrations of 25 and 30 weight % in PETT, that can be identified (arrows) in the morphology gradient of the PETT/RTM6 interphase.

Since the observation of the diffusion front was not possible, we measured instead the length of the inter penetrating network (IPN). Figure 3.5 shows the influence of the pre-curing on the length of the IPN : it varies linearly with the conversion rate before co-curing.

The characterisation of PETT-RTM6 interphases showed a symmetrical profile : two sea-island morphology separated with a co-continuous phase. The length of inter-

Sample	Elapsed cycle time at pouring (min)	percentage of pre-reticulation	IPN length (microns)
1	55	30	50
2	59	40	36
3	63	50	22

Table 3.1: List of the samples prepared for the analysis of the influence of the initial conversion of the resin at the beginning of the co-curing on the length of interdiffusion. Since the total length of interdiffusion is not clearly defined, this analysis is based on the length of the co-continuous phase observed.

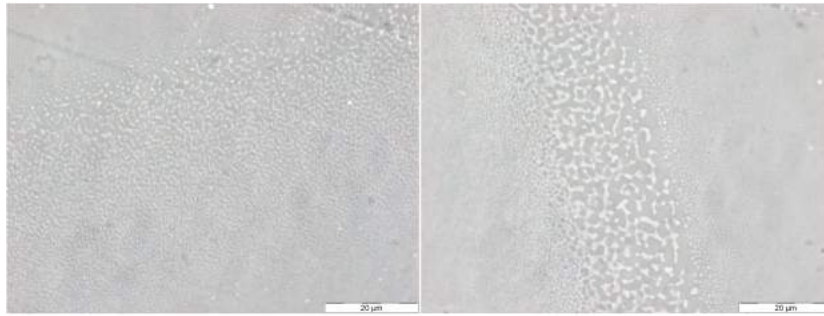


Figure 3.4: Microscope observations of the interphase formed by the cocuring of PTT films with the RTM6. The left picture, shows a co-continuous network wider than the right one for with the pre-curing was longer.

diffusion is expected to be large compared to the ones with PEI TP. To compute this length, we considered a linear diffusion, and homogeneous samples were prepared in order to identifying their structure among the profile. It has also been shown that an accurate control of the length of the length of interdiffusion as well as the co-continuous network is possible, the later ranging

## 3.2 Mechanical tests results

### Compression test

In order to deeply understand the damage mechanisms, compression tests on the homogeneous samples were performed. Figure 3.6 show the result on the sample tested. The true stress was computed via the engineering stress thanks to the equation 3.2, as well as the true strain thanks to the equation 3.1 :

$$\epsilon_{true} = \ln(1 + \epsilon_{ing}) \quad (3.1)$$

$$\sigma_{true} = \sigma_{ing}(1 + \epsilon_{ing}) \quad (3.2)$$

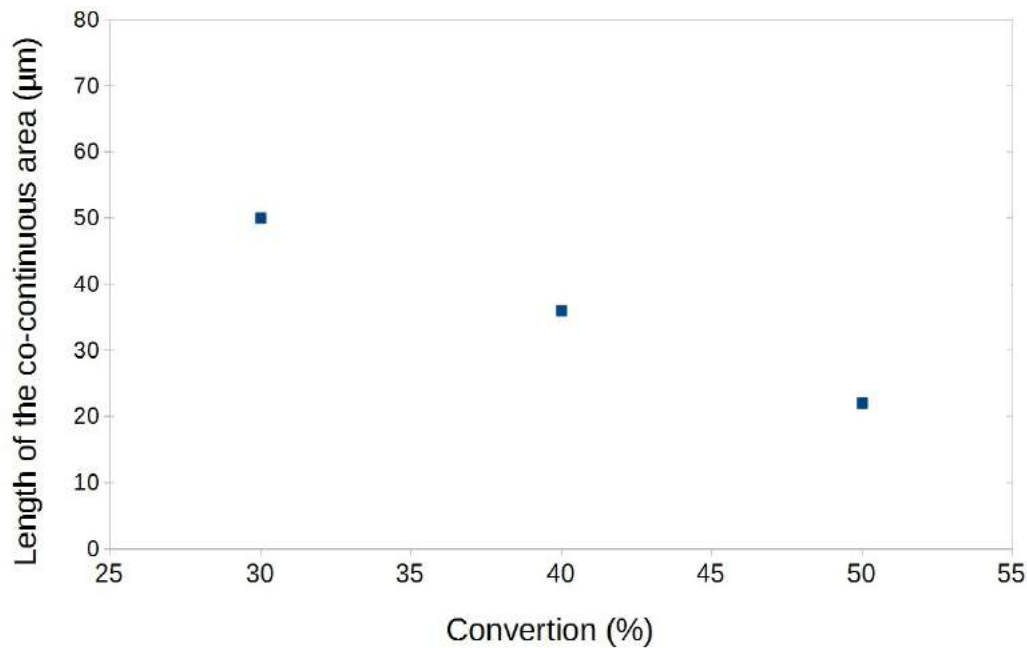


Figure 3.5: Evolution of the length of the co-continuous area as a function of the resin conversion. The length of the co-continuous domain tends to decrease linearly with an increasing percentage of pre-reticulation of the resin. An experiment giving results diverging from the other results was neglected

Unfortunately, no samples of 25 % of thermoplastic are available despite many attempts in preparing it.

The transition between the elastic and plastic behavior is not easily discernible. To fix this problem, we considered first the elastic limit at the stress value for which a release of the loading leads to 0.2 % elongation [21]. To do so, we computed the slope of the surely linear part of the curve. Then, the intersection point between the curve and a line with the same slope but an starting at  $x=0.002$  (i.e. 0.2%). Figure 3.7 shows the results of yield strengths, as well as a comparison with the rule of mixing.

The resulting elastic limit has increased compared to the rule of mixtures. There is probably a synergy effect. This effect might explain the results already obtained in the work of Quentin Voleppe, i.e. an effective toughening of the interface for PEI-RTM6

### Nanoindentation results

To complete the understanding of PEI fracture mechanism and the compression tests, indents were performed on the samples listed table 3.2

Figures 3.8 and 3.9 show the results provided by the experiment for the pure resin :

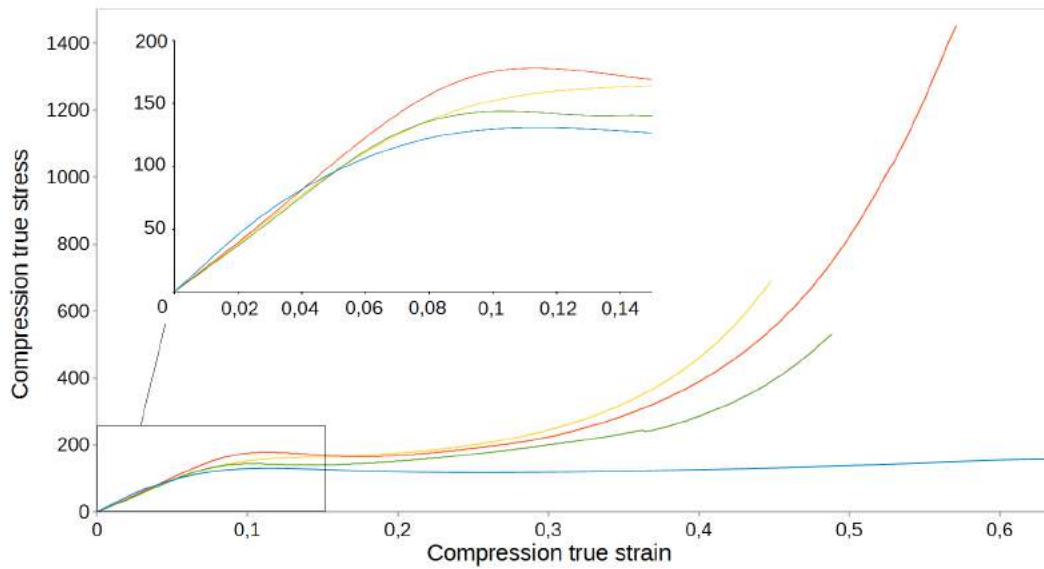


Figure 3.6: Compression results : the adding of PEI provide better mechanical properties than the mixing rule, a synergy effect is expected.

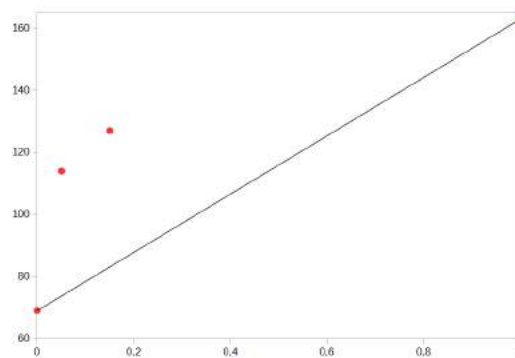


Figure 3.7: Compression results : plotting of  $\sigma_y$  as a function of the PEI content in weight percent

Sample  
 Pure PEI  
 Pure RTM6  
 RTM6 - 5pc PEI  
 RTM6 - 15pc PEI  
 RTM6 - 25pc PEI

Table 3.2: List of the samples prepared for the nanoindentation test

from the load displacement-curve, the hardness-displacement curve is computed. We can observe here that the hardness value is stable for a displacement greater than 1000nm. It was observed for all the samples, but some of the tests performed seemed failed. In order to calculate the hardness of one sample, an average of the hardness was taken from 1000nm to 2000nm in the reliable region, for each test. Then an average over the 16 tests was calculated. In the case test failed, corresponding results were not taken into account for the computation of the average since the obtained values was absurd.

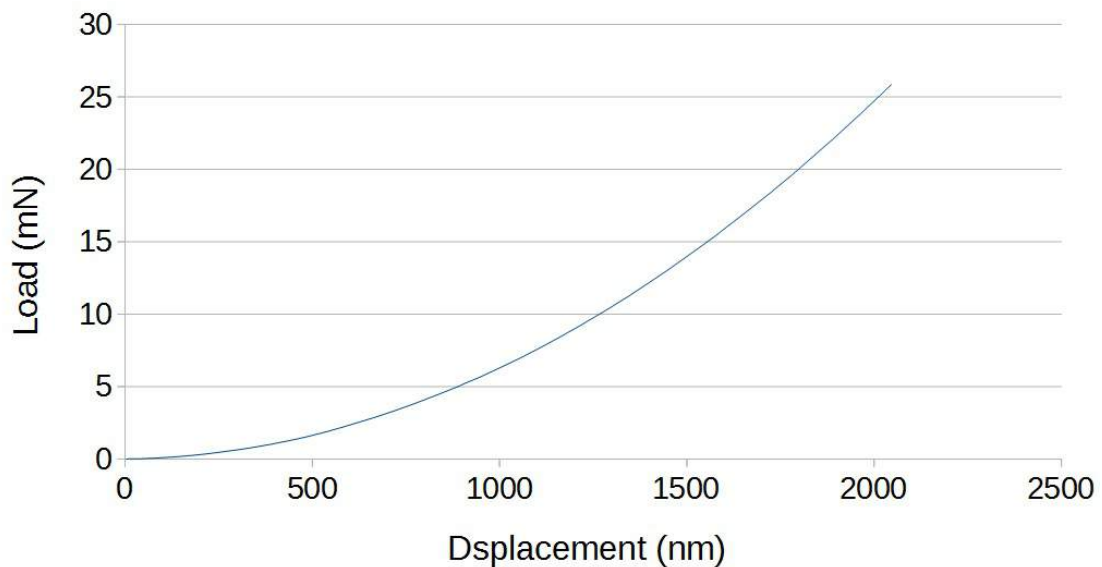


Figure 3.8: Load applied on the sample with the tip as a function of its depth of penetration (mettre toutes les courbes)

It was assumed that the yield strength was equal to the third of the hardness computed by the experiments  $\sigma_y = \frac{H}{3}$ , and figure ?? shows the yield strength evolution as a function of the composition of the RTM6-EI mixture in PEI weight percent.

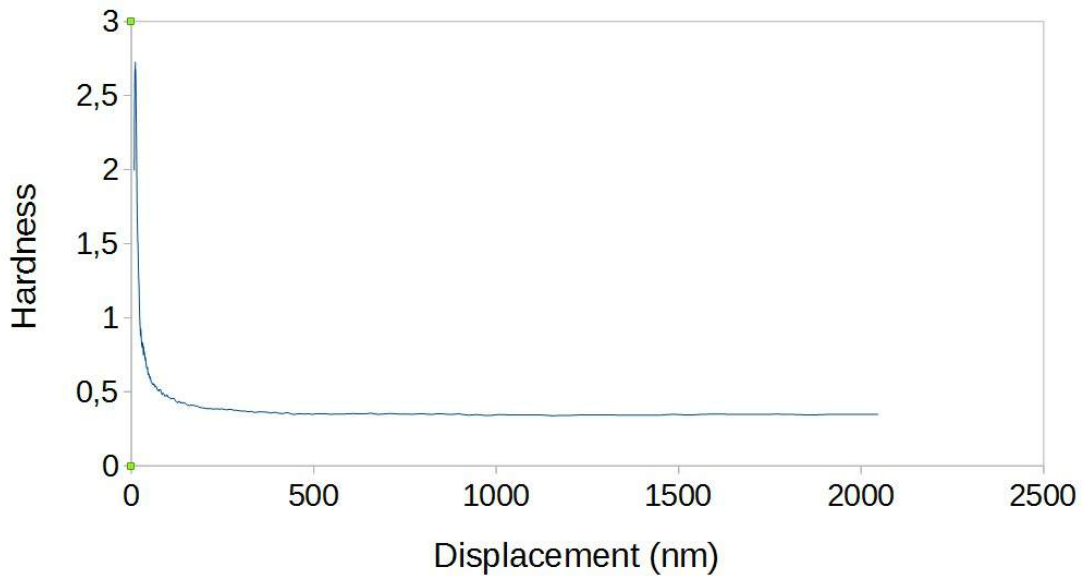


Figure 3.9: Load applied on the sample with the tip as a function of its depth of penetration

The same trend is observed for the nanoindentation and the compression tests using the definition of the 0.2 % yield stress. Despite the same trend observed, discrepancy are observed between the results from the compression test and the ones from the nanoindentation tests: the later gives results with a lower yield stresses. However, the first assumption  $\sigma_y = \frac{H}{3}$  was coarse and for polymers  $\sigma_y$  can be computed by  $\frac{H}{\alpha}$  with  $\alpha < 3$  [35].

As it is showed in Figure 3.10, a value of  $\alpha=2.25$  lead to a good enough fit of the

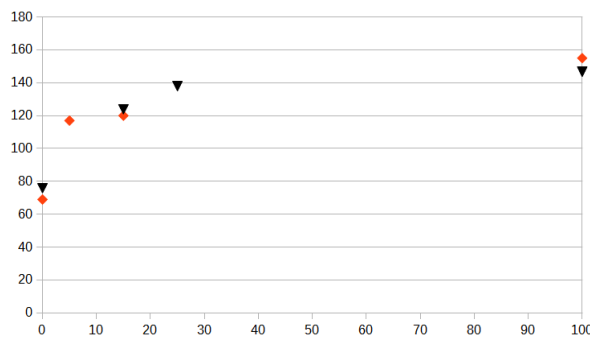


Figure 3.10: Nano-indentation results compared with the compression results : computed  $\sigma_y$  as a function of the weight percent in PEI a parameter  $\alpha = 2.25$  allows a correct correlation of the two experiments.

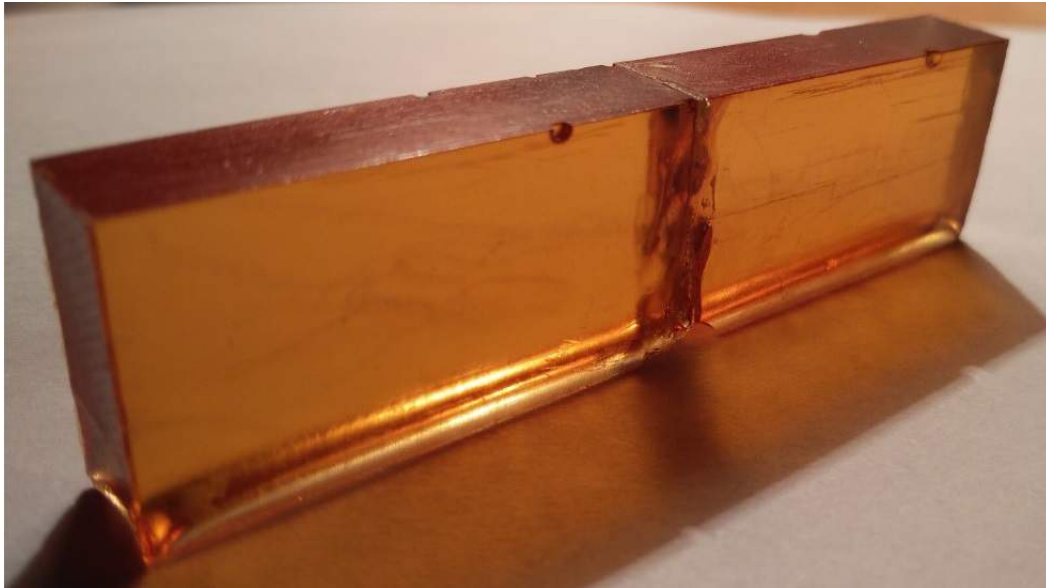


Figure 3.11: Picture of SENB samples not yet machined. The thin film has subsided because of both the high temperature allowing flowing and the stress exerted by the old on the film, making it bend.

compression curves and the indentation cures. The association of the two methods allows to affirm that there is a synergic effect by adding the thermolastic to the resin.

### **SENB tests**

After the preparation of the SENB samples, the first observations made are the deformation of the thin film upon curing. Unlike PEI films which remained straight, PETT films subsided. It is due to the tightening of the mold, pressing the PETT thin film. It engenders stresses among it. This stress make the PETT film go out from the mold at higher temperatures where the TP can flow, and push on the film in the space dedicated to the sample, bending the film. To successfully avoid this phenomena, thin films and the mold were heated up to 180 and built at this temperature. It reduced this phenomena, as it is showed in Figure 3.11, in which the film remained in the mindle of the sample. However, an other problem was encountered: indeed, bubbles formed at the interface. It probably comes from the PETT film itself, in which micro-bubbles probably formed during the thin film preparation with the press. Such micro-bubbles would agglomerate and form macrobubbles, as it is illustrated in Figure 3.12.

The mechanical tests still have to be performed. However, the observation of the samples allows to assume that the test result of these samples will not be the intrinsic properties of the interphase due to the presence of bubbles.

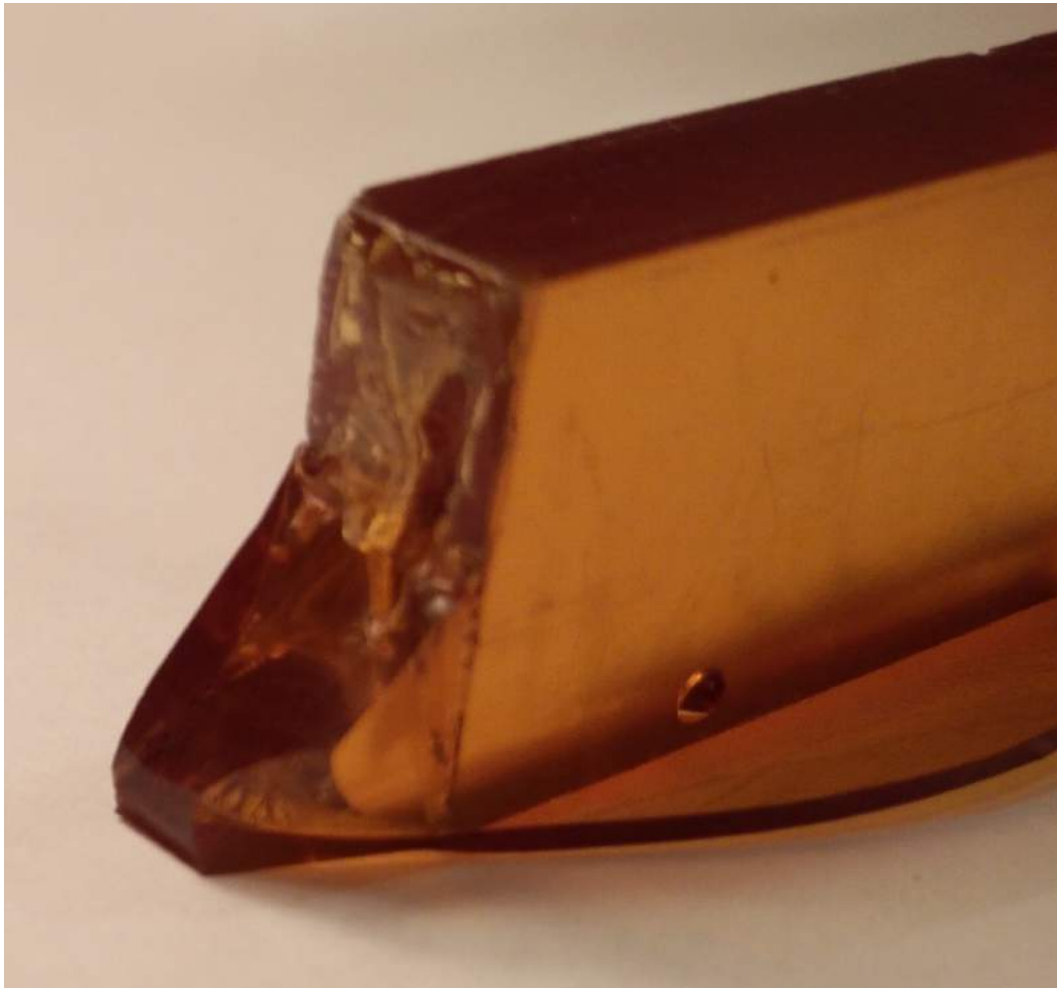


Figure 3.12: Picture of a broken SENB sample. The sample broke before testing. One can observe a bubble at the middle of the interface. It contributed a lot to the weakening of the interface

## 4 Influence of the patterning

---

Since optimum parameters were already defined, we continued this study by analysing the effects of the roughness of the thermoplastic thin film, and the first step consisted in patterning the film. The main parameter in the study of the influence of patterning of the TP on the mechanical properties of the TP/TS interphase is the size of the smallest repeated feature, that we called the patterned feature size. A range of feature size of the pattern was assessed regarding the length of interdiffusion. Indeed, a too wide patterned feature size would tend to have properties similar to an initial plane interface. On the other hand, a too small pattern feature size can vanish because of the interdiffusion process and swelling.

Knowing that the interdiffusion length (from front to front) of PEI/RTM6 interphases is of the order of tens of microns [16], the chosen feature size was of the order of 100 microns, to obtain hypothetically the structures showed in Figure 4.1.

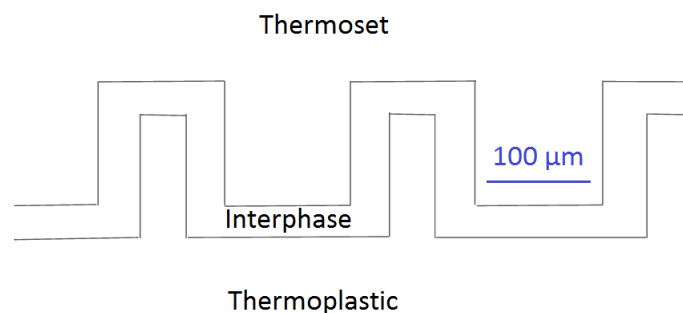


Figure 4.1: Scheme of the aimed TP-TS interphase with a rough thermoplastic layer. the feature size is 100 microns in this picture.

Such a feature size is too large for AFM patterning methods and the idea was to create a mold, for example by laser etching on steel, in order to press PEI films and have the desired the shape. However, this would require to prepare a mold for all the different patterns that we want to study, making this solution too expensive. This is why the patterning was done directly on the thermoplastic film with a laser on top of the polymer. Another alternative we found to directly pattern the TP thin film is 3D printing. 3D printing offers many advantages for the shaping, since it allows an accurate control over the structure we want to obtain, down to the tens of microns.

However, due to the high Tg of PEI, we could not use this polymer with the 3D printer, since the process requires to be above the Tg for tens of degrees, temperature not reached by the 3D printer available. In order to study the influence of the patterning on the mechanical properties of the TP-TS interphases, two different methods for patterning were explored.

### 4.1 Laser patterning

The patterning of PEI samples was done with the laser.

#### **influence of the parameters**

The main parameters for the surface patterning are :

- the laser power, ranging from 0 to 2000 mW
- the remaining time, which is the time for which the laser beams on the same point
- the number of paths accomplished for each points

Batches of experiments were performed modifying the three parameters described before. To analyse the influence of each of them, tests consisted in fixing two parameters and make the third one varying.

Several observations were made :

- The first remark we can make is that because of the PEI thin film transparency, etching was sometimes non uniform, depending on the surface on which relied the thin film. Indeed, sometimes etching occurred at the top surface at the incidence of the beam, and sometimes on the other side, even among the same line patterning. To fix this problem, a steel plate was placed under the film.
- The second remark is that the laser focusing was set by hand in order to make the dot formed by the laser beam as small as possible on top of the surface. It is probably not the best experimental set up since the depth of field have to be taken into account. Intuitively, the depth of field should have an influence on the shape of the pattern profile.
- The third remark is that for a power at intermediate values between values for which it etches and values for which it does not etch, over the same tests, sometimes it etched, sometimes it did not. However, it was observed that a

defects on the film such as an already etched area on the film help the etching start. For reproducibility, a "starting" line was etched to ensure the start of the etching -if possible- at these intermediate powers, as it is shown with the green bar in Figure 4.2.

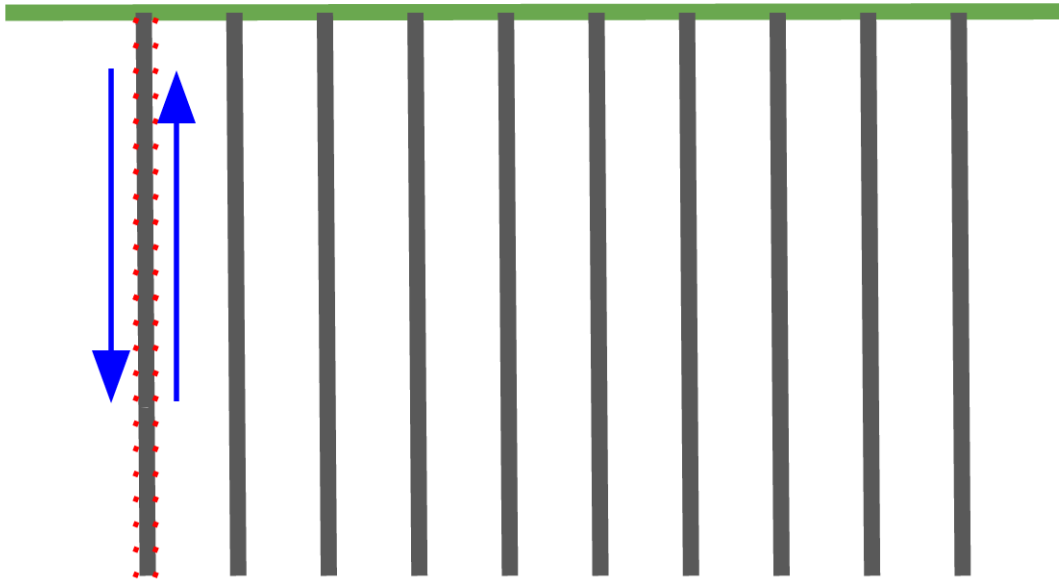


Figure 4.2: Scheme of the path followed by the laser : red dots highlight the area beamed by it. The blue arrows show the direction of the laser, going through borders of the drawn pattern in grey. The green bar represents the pre-patterning allowing a homogeneous pattern over the whole pattern.

For a too high power, even with a short remaining time, the polymer degrades and the lines where the laser etched the surface is partially burnt. It is easily observable since it is black. On the other hand, a too low power does not even pattern the surface. This result is also observed with the remaining time, considering the power range for which the laser does etch the surface. Finally, the influence of the number of paths seems similar to the remaining time, but different results were found for experiments having the same cumulated time spent beaming the same dot at the same power, but with different numbers of passages. This is due to the fact that for several passages, the sample cools down between two passages and part of the time of the next passage is needed to heat up again. Also, the remaining time affects neighbouring points, a side effect that can be counterbalanced by the number of paths accomplished. We expect that burnt samples won't affect the properties since only a very small part of the line

## Influence of the patterning

---

is burnt and since these burnt molecules are at the surface and will be the ones that will diffuse far from the initial interface, and then not interacting during the fracture process for SENB tests.

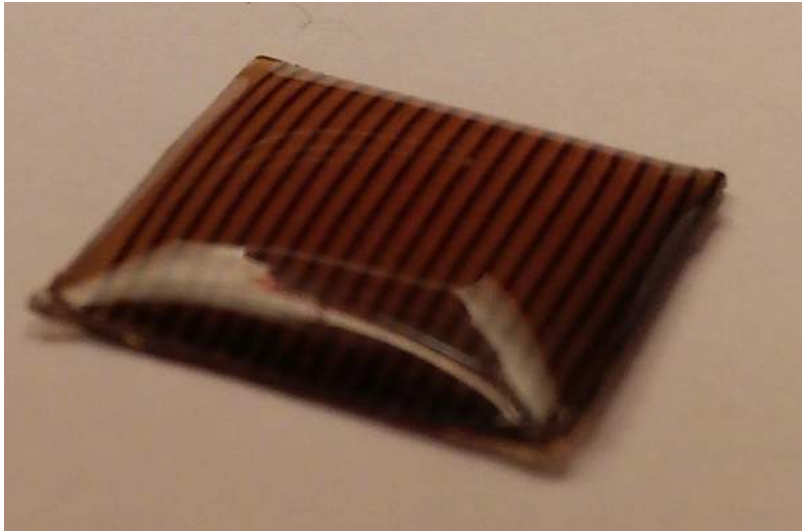


Figure 4.3: Picture of a resin cured upon a patterned PEI film : the burn lines are visible, in dark lines.

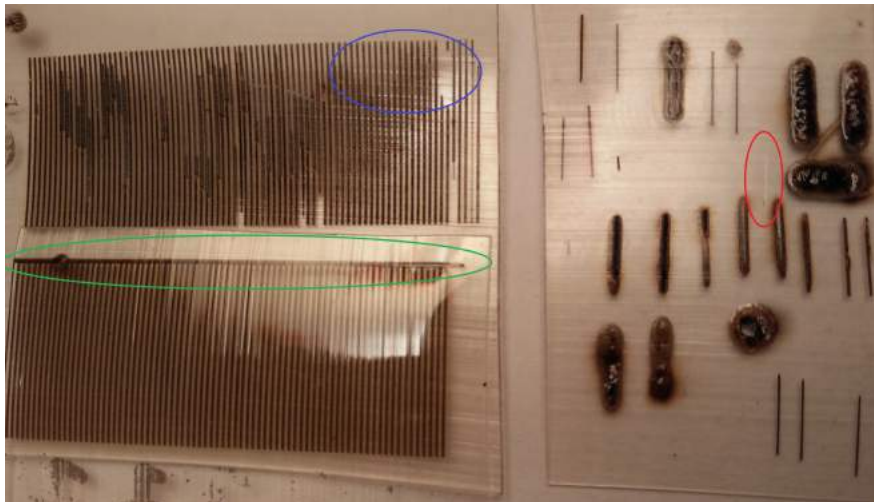


Figure 4.4: Several patterns performed with the laser, where only the beam power varies. One can see, circled in red, a very thin and not burnt patterned line, best resolution obtained up to know without apparent degradation. Circled in blue, one can observe defects on the pattern, avoided by the use of a pre-patterned line at high power, highlighted in green.

## 4.2 Patterning via 3D printing

PETT films were printed with the Markerbot Replicator in order to prepare SENB samples. The shape of the thins films is illustrated in Figure 4.5.

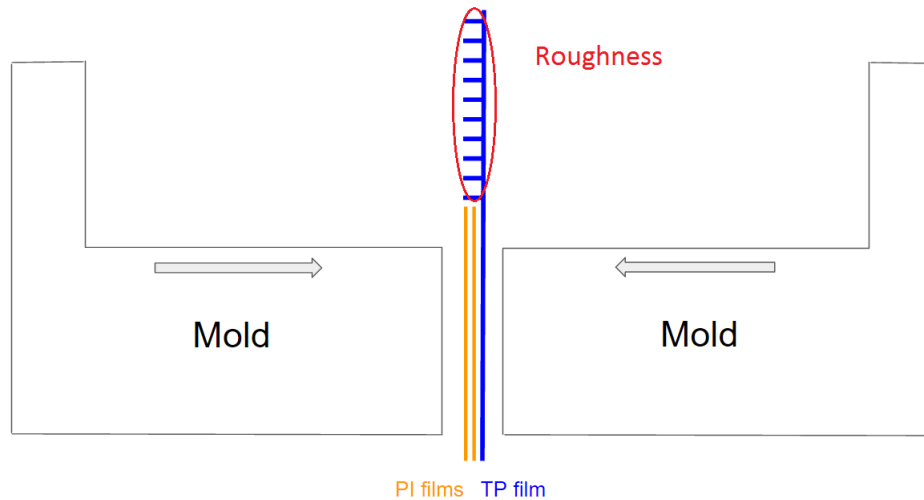


Figure 4.5: Scheme of the SENB samples preparation, with patterned PETT films

## 4.3 Characterization of the interphases

No characterisations were performed yet on these samples. However, some observations can already be done by looking at the SENB samples made

**SENB tests** The step of deposition of the crenelled film at 180C on the mold as it was done for flat interfaces was not possible because the film bent at 180C, due to the pattern. This step was skipped. The problems encountered for the flat thin film surfaces were also observed here, namely the thin film subsiding and the bubbles. However, the reasons differ from before. Indeed, the bubbles can come from :

- the PETT film itself, in which microbubbles formed during 3D printing
- bubbles trapped between the PETT film and the PI film. Indeed, the printing induces defects due to the smallest resolution. The surface is not perfectly flat where it should be, so that the PI film does not fit perfectly with the PETT film.

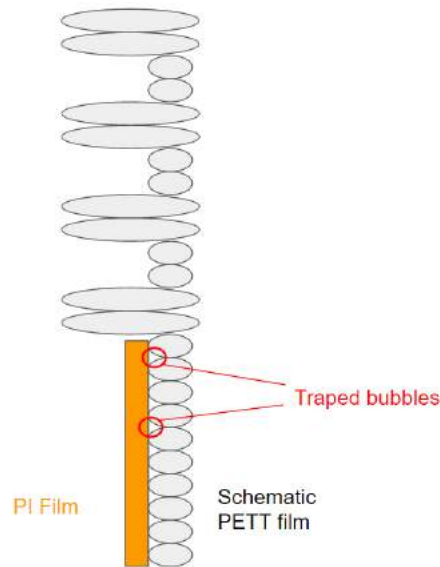


Figure 4.6: Detailed scheme of a PETT film: each layer is illustrated by a grey oval. One can see that the PI film, as a flat thin film, does not fit well the thermoplastic film

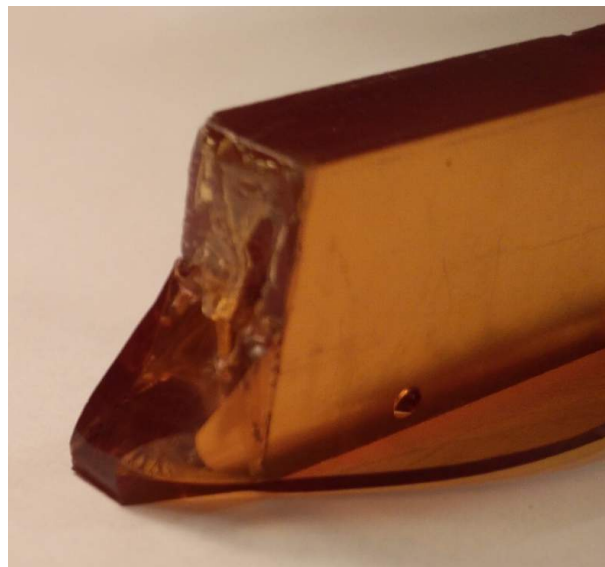


Figure 4.7: Picture of a broken SENB sample. One can observe the presence of bubbles inside the crack surface.

## Conclusion

---

Following the work of Quentin Voleppe, mechanical tests performed on homogeneous RTM6/PEI blends samples showed a synergic effect in the addition of the PEI into the RTM6 matrix, and the results were supported by two different mechanical

characterisations. In order to even more increase the damage resistance of the interface, roughening was also introduced to PEI thin films by the use of a laser in order to create new mechanisms promoting energy dissipation. Patterning by laser turned out to be a fast patterning method as well as a versatile one since many parameters are available to tune the experiment and so the obtained pattern. However, this study had to abort due to technical issues, despite promising preliminary results on the patterning of the PEI films.

A new study of TS-TP interfaces was thus started with a low Tg polymer TP, namely PETT, in order to compare its TP-TS interface mechanical properties with the ones of PEI, a high Tg polymer. First, a control of the interdiffusion length was done successfully and the co-continuous area varies linearly with the pre-conversion of the resin. This control would allow to tune the interphase mechanical properties for further experiments. The obtained morphologies differ since a sea-island morphology and a wide co-continuous area only were observed, while PEI distinguishes by the presence of a cellular structure and a narrow co-continuous domain. The low Tg PETT should promote the fracture resistance by the formation of the co-continuous network, and the long interdiffusion area formed due to its diffusion mechanism above Tg. On the other hand, the cellular morphology, suspected to be one of the key morphologies in the increase of damage of interfaces, is observed in PEI systems and cannot occur with the PETT.

PETT was wisely chosen as it can be 3D printed, allowing us to continue the study of the effect of the surface roughness. However, problems in the preparation of SENB samples as well as a lack of time made this study aborted.

Homogeneous samples for SENB tests are already ready to be tested, in order to determine the influence of the content in PEI on the energy release rate. The computation of the energy release rate as well, as the observation of the fracture surfaces for the identification of the crack mechanism, as a function of the PEI content, should end the mechanical study of PEI-RTM6 interphases. Further studies must be carried out in order to compute the mechanical properties of the TP-TS interphase with PETT, i.e. the elastic properties and the fracture properties. The observation of the failure surfaces should provide more information for the fracture mechanism also, especially on the promising co-continuous network. Moreover, more refined characterisations

## Influence of the patterning

---

such as Raman spectroscopy to determine the total diffusion length still have to be performed.

## References

---

- [1] R. COURTEAU. Les perspectives d'évolution de l'aviation civile à l'horizon 2040 : préserver l'avance de la France et de l'Europe. June 2013.
- [2] J. Pora. Composite materials in the Airbus A380 - from history to future - . .
- [3] G. Ciba. User's guide to adhesives.
- [4] D. Dumont, D. Seveno, J. De Coninck, C. Bailly, J. Devauxa, and D. Daousta. Interdiffusion of thermoplastics and epoxy resin precursors: investigations using experimental and molecular dynamics methods. *Polymer International*, 61(8):p 1263–1271, August 2012.
- [5] R. Paton, M. Hou, A. Beehag, and P. Falzon. A breakthrough in the assembly of aircraft composite structures. 25th international congress of the aeronautical sciences.
- [6] R. C. Don, S. H. McKnight, D. Wetzel, and J. W. Gillespie Jr. Application of thermoplastic resistance welding techniques to thermoset composites. proceedings of the 52nd annual technical conference (1994) 1295-1297. Proceedings of the 52nd Annual Technical Conference 1295-1297., 1994.
- [7] B. Lestriez, J-P Chapel, and J-F Gérard. Gradient interphase between reactive epoxy and glassy thermoplastic from dissolution process, reaction kinetics, and phase separation thermodynamics. macromolecules. *Macromolecules*, (34): 1204–1213., 2001.
- [8] M. Hou. Thermoplastic adhesive for thermosetting composites. Material Science Forums 706-709 (2012) 2968-2973.
- [9] K. T. Botelho and al. Toughness enhancement of the rtm6 system employing thermoplastics and block copolymers. .
- [10] M. L. Huggins. Some properties of solutions of long-chain compounds. *Journal of Physical Chemistry (1942)*, (46):151–158, 1942.
- [11] P. J. Flory. Thermodynamics of high polymer solutions. *Journal of Chemical Physics*, (10):51–61, 1942.
- [12] A. Morris Ad. Aina and al. Dissolution behavior of poly vinyl alcohol in water and its effect on the physical morphologies of PLGA scaffolds. *UKPB*, 2014.
- [13] C. Bailly. Lecture - polymer materials. .
- [14] P. J. Flory. Principles of polymer chemistry. Cornell University Press (1953).

## REFERENCES

---

- [15] C. Wilkies . L. A. Utracki. *Polymer Blends Handbook - Thermodynamics of Polymer Blends*. Springer, 2014.
- [16] Quentin Voleppe. *Characterization and modelling of the microstructure and cracking resistance of thermoset/thermoplastic interphases - application to thermoset composite welding*. PhD thesis, Université Catholique de Louvain, 2016.
- [17] P. G. de Gennes. Reptation of a polymer chain in the presence of fixed obstacles. *Journal of Chemical Physics*, 55:572–579., 1971.
- [18] G. S. Park. An experimental study of the influence of various factors on the time dependent nature of diffusion in polymers. *Journal of Polymer Science*, 11: 97–115, 1953.
- [19] G. S. Park J. Crank. Diffusion in high polymers : Some anomalies and their significance. *Transactions of the Faraday Society*, 47:1072–1082, 1951.
- [20] A. H. Windle N. L. Thomas. A theory of case ii diffusion. *Polymer*, (23):529–542., 1982.
- [21] T. Pardoën. Introduction to the deformation and fracture of materials. Lecture, 2015.
- [22] Mark W. Denny Katharine J. Mach, Drew V. Nelson. Techniques for predicting the lifetimes of wave-swept macroalgae: a primer on fracture mechanics and crack growth. *Journal of Experimental Biology* 210: 2213-2230, 2007.
- [23] M. Braccini and M. Dupeux. *Mechanics of Solid Interfaces*. Wiley, 2012.
- [24] C. Atkinson. On stress singularities and interfaces in linear elastic fracture mechanics. *International Journal of Fracture*, pages 807–819., 1977.
- [25] J-P Chapel C. Plummer B. Lestriez, J-F Gérard. Maîtrise de la morphologie et de l'adhésion aux interfaces macroscopiques thermoset/thermoplastique. matériaux. *Matériaux*, 2002.
- [26] S-C Kim Y-S Kim. Properties of polyetherimide/dicyanate semi interpenetrating polymer network having the morphology spectrum. *Macromolecules*, (32):2334–2341, 1999.
- [27] *HexFlow® RTM 6 - Product Data - 180°C mono-component epoxy system for Resin Transfer Moulding and Infusion technologies*.
- [28] Svetlana TEREKHINA. *Comportement en Fretting du Composite CFRP Hextool et de sa Matrice Bismaleimide*. PhD thesis, Ecole Centrale de Lyon, 2011.
- [29] M. J. Marks HAa Q. Pham. *Ullmann's encyclopedia of industrial chemistry*. Dow Chemical.

## REFERENCES

---

- [30] Taulman. Taulman3d” releases “t-glass” industrial 3d printing material. . URL <http://taulman3d.com/t-glase-features.html>.
- [31] Safari books online. Basics of fused deposition modeling. . URL <https://www.safaribooksonline.com/library/view/3d-printing-for/9781783550753/ch01s04.html>.
- [32] ASTM Standard D 5045-99. Standard test method for plane-strain fracture toughness and strain energy release rate of plastic materials. annual book of astm standards (1999). .
- [33] Anthony C. Fischer-Cripps. *Nanoindentation, Third edition*. Springer, 2011.
- [34] . Astm standard d 695 : Standard test method for compressive properties of rigid plastics. annual book of astm standards (2002). .
- [35] S. Seidler T. Koch. Correlations between indentation hardness and yield stress in thermoplastic polymers. *Strain*, 45:26–33, 2008.

